Doctoral Dissertation
Doctoral Program in Electrical, Electronics and Communications Engineering
(33th Cycle)

Graphene as an active material for sensors and other devices

Implementation and optimization of graphene transfer process and functionalization for the fabrication of devices from FETs to Schottky Diodes

Alberto Ballesio

* * * * * *

Supervisors
Prof. Fabrizio Pirri, supervisor
Prof. Gianluca Ciardelli, Co-Supervisor

Doctoral Examination Committee:
Prof. Stefano Cabrini, Referee, Molecular Foundry Berkeley
Prof. Victor Erokhin, Referee, IMEM-CNR Parma
Prof. Paolo Olivero, Committee member, Università di Torino
Prof. Matteo Bosi, Committee member, IMEM-CNR Parma
Prof. Sergio Ferrero, Committee member, Politecnico di Torino

Politecnico di Torino
March 2021

I hereby declare that, the contents and organisation of this dissertation constitute my own original work and does not compromise in any way the rights of third parties, including those relating to the security of personal data.

…………………………………..…

Alberto Ballesio
Turin, March 2021

Summary

The present work deals with the study of graphene for the fabrication and optimization of graphene Field Effect Transistor (G-FETs) for sensing purposes, with a focus on the transfer process of graphene and on its functionalization.

Two parallel research activities were carried out, the first regarding the process for the fabrication of the device, with its optimization and preliminary tests, and the second regarding the functionalization of graphene for the specific detection of the analytes required.

The work started with the design of the transistor and the study of the best configuration for the sensing. The path chosen was the electrolyte gated transistor, which allows the solution under test being an active part of the device and strongly influencing the measurements.

The transistor was then fabricated, following standard lithographic processes and the techniques commonly used in literature for the growth and the transfer of graphene on the device. Standard measurements were performed to test the device behavior and compare it to other G-FETs reported in the literature.

The next step was to improve the G-FET fabrication: while the lithographic steps are extremely standardized for the device fabrication, the graphene transfer process remains one of the main limits for its implementation in mass fabrication.

Graphene was then transferred using a technique usually employed in the microfluidic field, the Hot Embossing. With a simple change of substrate, from Si/SiO_2 to Cyclo Olefin Copolymer (COC), it is possible to imprint graphene into it due to its polymeric nature. Being the substrate a polymer, if thin enough it results to be also flexible, an interesting improvement that can increase the fields where graphene can be employed.

The G-FETs successfully fabricated this way were tested and compared with the previous ones. Their sensing capabilities were also investigated with simple pH

and stress measurements, in order to understand their eligibility for the biomarkers and antibiotics sensing.

The new transfer process was then tested for the fabrication of other devices. Due to the transparency of the substrate, the best application was in the optics field. A graphene Schottky diode was then fabricated and tested for its behaviour compared with previous literature.

In parallel, the functionalization protocol for the sensor was studied. Graphene is a good candidate for the functionalization with the probe that will selectively capture the analytes that need to be detected. Different molecules were taken in consideration for the bonding, and after some preliminary tests Caffeic acid was chosen for the study.

A functionalization protocol was defined for the molecule, and Raman characterization was performed to establish the successful bond of a monolayer on the graphene structure. Few other molecules were tested to increase the range of functionalization possibilities, but the results are still preliminary and further investigation is required.

Acknowledgment

Thank you to my supervisor.
Thank you to the people who helped me for this work.
Thank you to the colleagues and friends who made the journey easier.
A special thanks to the people at Politecnico di Chivasso.
Thank you, Eve.
Thank you to my friends.
Thank you to my family.

To those who always
support me with their
words, with their
actions and with their
thoughts.

Contents

List of Tables

List of Figures

1 Chapter

Introduction

1.1 Research context and motivation

The following research work started three years ago with the purpose of investigating the exploitation of graphene in the biomedical and electronic fields. The attention on graphene from the research community has been very intense in the last few decades due to its outstanding physical performances, allowing an always deeper comprehension of its properties. The drawback of this material was the difficulty of its implementation in an industrializable process.

In the last years due to the increasing interest in the biomedical field and in “green” electronics, the exploitation of graphene for electrical bionsensors and electronic devices with an organic active material has attracted the interest of many researchers, together with the possibility of functionalizing it for better sensitivity and detection results.

In this work, the idea was to follow this trend while improving one of the critical aspects of graphene: its transfer from the growth substrate to the final device. Starting from the understanding of the state of the art of graphene electrical sensors, the effort was addressed to develop a robust process that could speed up the fabrication without impacting the performances.

The activities behind this research were not only driven by personal interest but were part of the “DEFLeCT” project, in the framework of the Piedmont “Health and Wellness” Platform. The acronym stands for Digital tEchnology For Lung Cancer Treatment: the aim is to develop different platforms (from different types of biosensors like electrical and electrochemical to Lab On Chips and Organ on chips) in order to increase the ability to early detect lung cancer and to get devices that will allow a better understanding of the disease and how to cure it.

Another project that partially covers the following work is the “Food-Drug-Free” project (Agri-Food Platform of Piedmont Region), which has the aim of detecting contaminants in edible products like milk, eggs and honey.

1.2 Aim of the proposed research

The aim of this three-year work was to exploit the properties of graphene to develop different electronic devices with a specific focus on biosensors. In order to do so, the fabrication process needed to be thought from the beginning and optimized to meet the performances requested by the project and the other groups (like biologists) involved.

For that a new process for the handling of graphene was needed, in order to help with the fabrication and further improve its potential, since the typical transfer with the help of PMMA had many issues that needed to be solved. With a new way of transferring graphene, other devices than the electrical biosensors (which were the main focus of the research) could get a benefit, and an improvement was found also in the exploitation of graphene for diodes.

The use of graphene in biosensors does not only require the optimization of its electrical behaviour, but also to address its surface chemistry: to provide a valuable sensor not only a proper electrical behaviour is needed, but also a suitable functionalization. For this purpose, in parallel with the study of the fabrication process, a study on the possibility to functionalize graphene and how to do it was performed, in order to achieve the best results.

1.3 Thesis outline

The following thesis is divided in three main sections: Theory, Materials and methodologies and Results and discussion. The first section is focused on outlining the background from which the work was started: from the processes to produce and transfer graphene known in literature to electronic devices using graphene already published, concluding with an overview of known procedures to functionalize graphene.

The following section analyses the materials and the processes used and studied in this research; the main topics here are divided into the core new graphene transfer and the functionalization. The first one is split then in the Biosensor part and the Schottky Diode one.

The results section is directly divided into the Biosensor, the Diode and the Functionalization part.

A final Conclusion and Future Outlooks section sums up the thesis findings and gives some ideas on how to further develop the work here described.

2 Chapter

Theory

As described in the introduction, the present work is focused on graphene and how to use it. In order to understand how to exploit it at its best, a thorough research was needed to investigate the material itself: how it is made, what are his characteristics, what are his advantages and disadvantages. After that, the need was to understand how it has already been employed in order to search how to improve it and maybe finding a not yet explored path, with a specific focus on which protocols and materials have already been used to functionalize it.

2.1 Processes for graphene production

It is well known that the first time graphene was produced was through a very simple method: mechanical exfoliation. Researchers simply used an adhesive tape and attached it to pyrolytic graphite. Due to the particular structure of graphite with many monolayers of sp^2 carbon atoms stacked onto each other, the tape was able to keep few layers from the graphite.

Graphene was the first truly 2D material[1], and from that moment many efforts were made to find cleaner and more reliable methods to produce monolayer or few layers graphene[2–5]. Here are described the most common and known production methods with their advantages and disadvantages, strongly based on the review "Mechanical properties of graphene and graphene-based nanocomposites"[6].

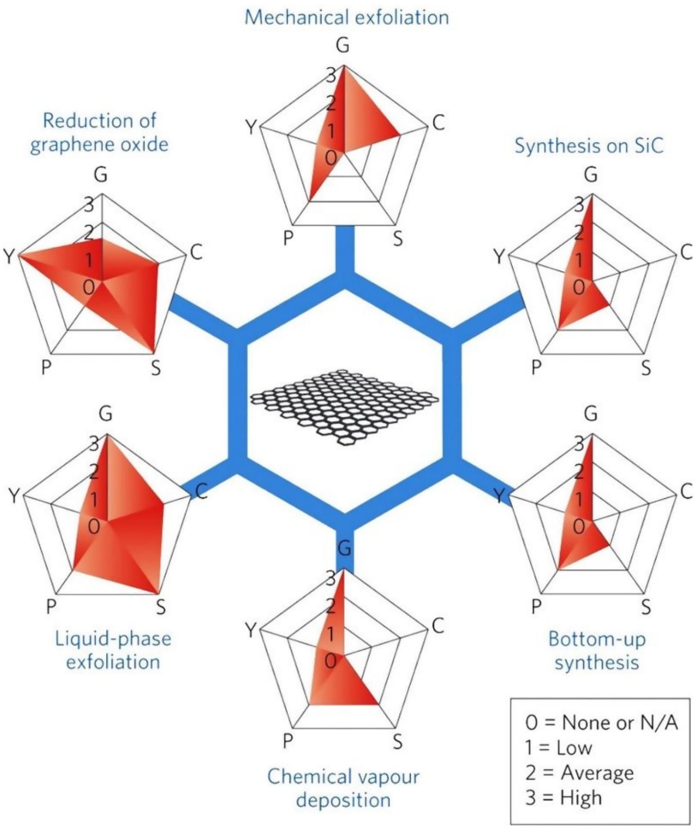

Figure 1 An overview of the common graphene production methods. G stands for the quality, C for the cost (where lower values corresponds to higher costs), S for the scalability, P for the purity and Y for the yield. (adapted from [7]).

2.1.1 Micromechanical exfoliation

This has been the first method used to produce graphene and is still one of the most commonly used by researchers and industry [8]. The technique is based on the exploitation of Van der Waals forces to remove layers repeatedly from a thin slab of pyrolytic graphite [9].

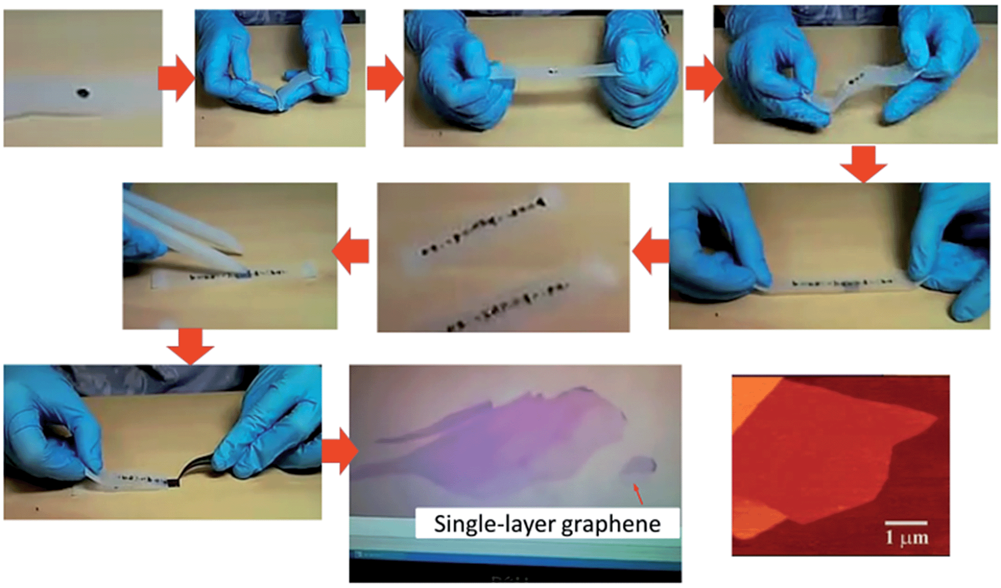

Figure 2 The steps required to obtain a single layer graphene with the micromechanical exfoliation method. (reprinted from [9])

The tape will attach to the first few layers and peel them away, thinning the main sample. By repeating the same process over and over, there will remain only ideally a single layer of carbon atoms and so a monolayer graphene.

The process is of course very dependent on different factors, and not extremely reliable. A lot depends on the adhesive tape selected for the process: the stickiness of the tape can result in stronger or weaker bonds with the graphite, thus influencing the number of layers removed at each passage and the quality of the final sample [10].

Another problem depending on the adhesive used is the presence of impurities, that will surely remain in the final sample and could be difficult to remove. The other important step is the transfer of the graphene on a selected substrate, and with this technique it results in the necessity to carefully remove the tape from the sample[10].

One of the main problems however resides in the difficulty to remove every layer except the last one to assure that only a monolayer remains: most of the time the final result is a few layers graphene, which still presents properties similar to the high-quality graphene, but not exactly the same [11].

2.1.2 Reduction of graphene oxide

In this case, the process revolves around exploiting the oxidation of graphene to exfoliate the layers from graphite and then reduce the graphene oxide to get back to the original graphene structure [12,13].

Different oxidation and reduction processes may be used and may range from thermal to chemical, affecting the final result [13,14]. Moreover, the different processes may exhibit strong differences depending on the parameters or materials used: in the case of the chemical reduction, the choice of the solvent, the reducing agent and the surfactant are fundamental to obtain a stable solution and a suitable result [15–18].

Many different defects may be present, both intrinsic and extrinsic: edges and deformations may appear in the graphene structure, as well as -O or -H groups remaining attached to the carbon atoms (Figure 3).

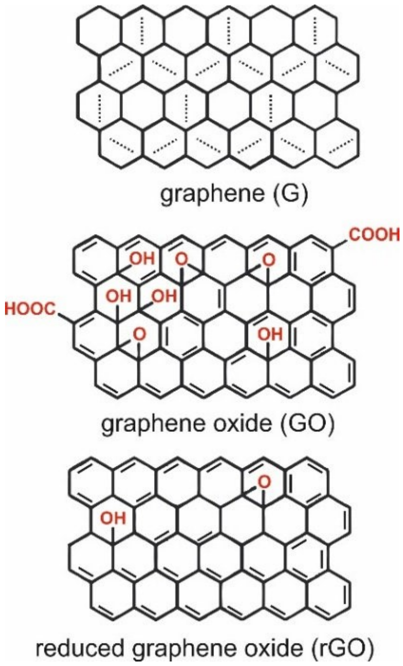

Figure 3 Differences between graphene, graphene oxide and reduced graphene oxide.(reprinted from [19])

This production process has the potential to be scaled-up, but the presence of defects and inhomogeneities in the graphene oxide structures may bring some difficulties and significant gap from the quality of other processes [6].

2.1.3 Liquid phase exfoliation

Liquid phase exfoliation is another very common production process and between the ones with the lower production costs [6].

It is based on three steps: first the graphite needs to be dispersed in a solvent or a surfactant, then it needs to be exfoliated and finally it needs to be purified to separate the exfoliated part from the non-exfoliated one. In the case it is requested in dry form, the solvent needs to be completely removed [20,21].

Many different liquids can be used for the dispersion, ranging from solvents to aqueous surfactants solutions, and can influence the final result of the process [6].

The sonication time can strongly influence the dimensions and the concentration of graphene, so a careful optimization needs to be performed: longer sonication times can increase the concentration but may produce smaller graphene sheets [22–24].

Finally, the purification is usually performed by ultracentrifugation, which allows removing thicker flakes. Also in this case the right compromise needs to be found, since a higher centrifugation speed means thinner flakes but also a smaller lateral size (Figure 4) [23].

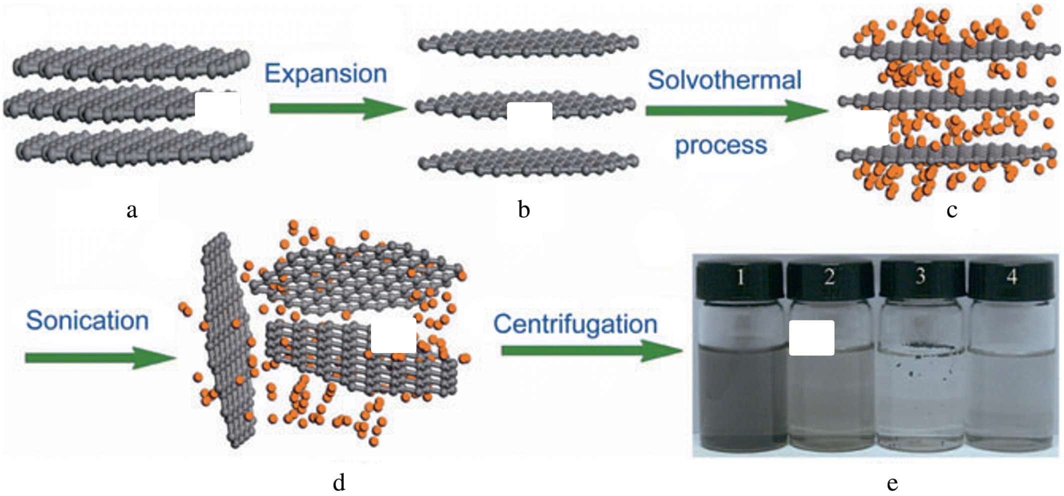

Figure 4 Graphical explanation of the liquid phase exfoliation passages. (adapted from [25])

From the upscaling point of view, this is probably one of the most promising techniques: it is very simple, fast and allows producing a high quantity of graphene in a small time. The downside resides in the quality, which can be comparable to the graphene oxide and remains quite lower than other techniques like CVD [26].

2.1.4 Chemical Vapor Deposition (CVD)

Chemical Vapor Deposition is probably the technique mostly used to produce very high-quality monolayer graphene. The downside of the process is the need of a metal substrate for the growth, which then requires a method to transfer the graphene on the chosen device [27].

There exists a range of different CVD methods but all share a common process: a seed metal substrate is heated up to high temperatures in a chamber which is injected with a flow of hydrocarbon precursors [28–30].

The decomposition of the hydrocarbons starts the nucleation of carbon atoms which then grow into larger domains. On some metal substrates, when the entire area is covered with graphene, the inertness of the material prevents the process to continue, ensuring the quality and the monolayer form of graphene (Figure 5) [27].

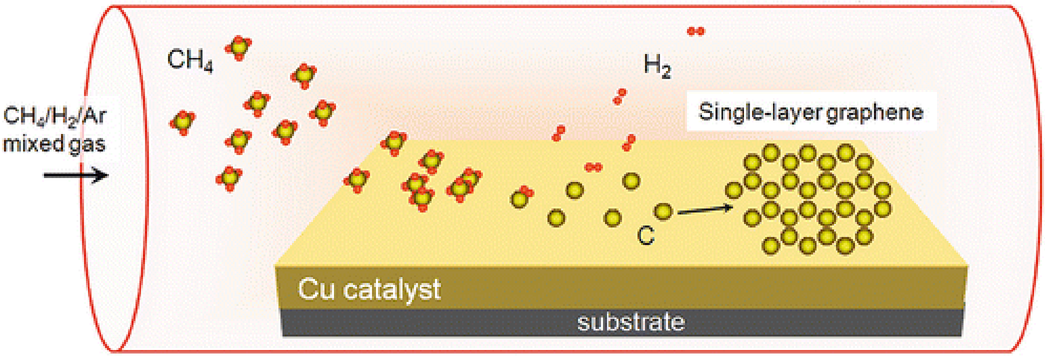

Figure 5 CVD graphene growth on Cu seed layer.(adapted from [31])

The inertness of the material is also the main disadvantage of this procedure, since the main difficulty resides in the need to transfer the graphene from the seed substrate to the required surface, and this process can create defects and wrinkles while also adding impurities [32].

This remains however the best process to produce the highest quality graphene on a large area, and for this reason was chosen for the work here described.

2.1.5 Bottom-up synthesis

Another possibility is to start from small but atomically precise building blocks and to attach them until the required structure, in this case graphene, is formed [33].

These blocks need to have specific parts that will be stimulated externally and will couple together in order to build the next unit, and so on until the final structure is reached.

Usually very high temperatures are required, and the external stimulus can combine and separate the building blocks to achieve the required structure.

With this technique, nanographene and graphene nanoribbons were produced, with a precise control of the atomic resolution [34–40].

While the obtained graphene has a very high quality thanks to the atomically precise control, the downside resides in the difficulties in handling and transferring it, alongside with the impossibility for a large-scale production with such a uniformity.

2.1.6 Electrochemical exfoliation

Also this approach starts from graphite and exfoliate it to obtain graphene, but in this case the exfoliation is performed in an electrolyte solution by imposing a current through graphite. The graphite, working as an electrode, is consumed and graphene is dispersed in the solution (Figure 6) [6].

Both the anodic oxidation and the cathodic reaction can be used for this process, with differences in the output characteristics and result [41,42].

While cathodic methods allow obtaining higher quality graphene with only few layers, the anodic ones are the most common in the literature but result in lower quality graphene with several layers and an oxidation state more similar to graphene oxide.

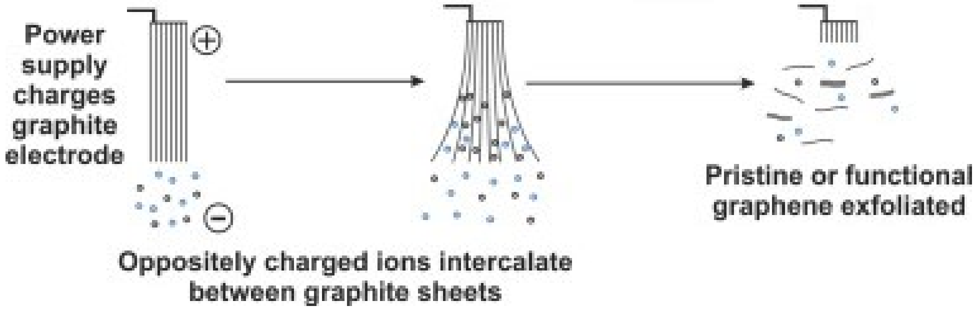

Figure 6 Electrochemical exfoliation of graphene. (adapted from [43])

The main advantage of this technique is that it can be performed in a single step and only minutes/few hours are required to be performed, in contrast with alternative methods. For this reason it could be suitable for scaling up the graphene production [44].

On the downsides, the electrolytes may be expensive and the low quality of graphene can prevent it to be used in some applications.

2.2 Graphene in transistors and other electronics

After its discovery, graphene has demonstrated to be an extremely versatile and useful material. Thanks to its properties and electrical characteristics, it has been exploited from the beginning in a range of different devices, trying to take advantage of the differences from a standard metal or semiconductor.

The following overview is based on the works from [45–47] which are reviews on the application of graphene in electronics fields, from transistors to sensors.

2.2.1 Graphene Field Effect Transistors (G-FETs) for RF

The high intrinsic mobility of graphene has always attracted the interest of scientists [48]. This characteristic can be extremely useful for Field Effect Transistors since allows a high switching speed, so the material was often used for this purpose [49,50].

A critical issue raised due to its ambipolar characteristic, for which it goes from conducting electron to conducting holes: the I_{ON}/I_{OFF} ratio was too low in comparison to the performances of a standard metal oxide semiconductor transistor.

For this reason scientists thought to exploit it in the RF field, which was dominated by high electron mobility transistors and required a low I_{ON}/I_{OFF} ratio, of the same order of magnitude of the graphene one [49,50].

The last problem is the reach of saturation current, which in graphene is almost impossible due to its high mobility. The solution resides in the creation of a band gap through doping and the exploitation of current pinch off effects (Figure 7)[49,50].

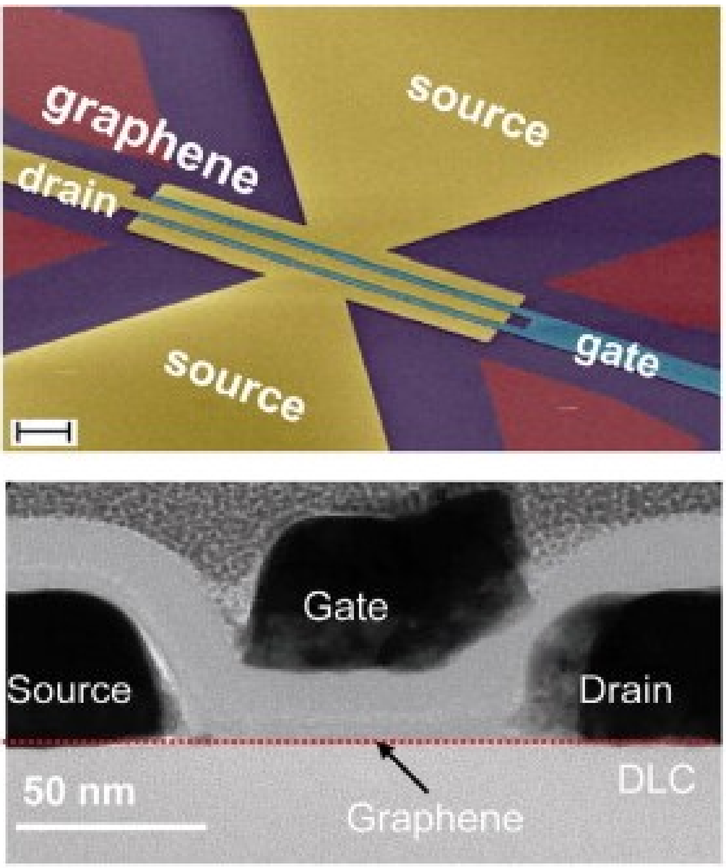

Figure 7 An RF graphene Field Effect Transistor and its FESEM image section. (adapted from [51])

2.2.2 Electro-Optical devices

Due to its optical properties, graphene has been also used for the fabrication of electro-optical devices (Figure 8).

Graphene can be used to absorb wavelengths from the visible to the mid-IR and can modulate the wavelength through electrostatic gating. The latter can interact with light by either working as an absorption modulating element and modulating the band gap width to reach a certain wavelength or modifying the graphene surface plasmon modes [52–56].

By exploiting graphene, also electronic fibers and tilted p-n junction switches have been fabricated, demonstrating how wide are the possibilities for this material [46].

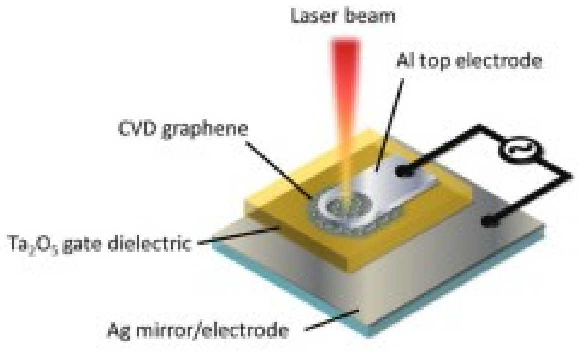

Figure 8 An example of graphene electro-optic modulator. (adapted from [57])

2.2.3 Infrared detectors

Graphene has also been used in the fabrication of infrared detectors (Figure 9)[58]. The two different types of detectors, based on thermal effects and on photon effects, have been both fabricated with graphene as active material.

In the case of thermal-based detectors, the IR radiation is absorbed and causes an increase in the material temperature, which then produces a change in some material characteristics which are temperature dependent, like electrical polarization in some cases or resistance in others. In the case of graphene, its photothermoelectric effect produces a net electric field [58].

In the photon-based detector, the photon is absorbed to create electron hole pairs and thus a photocurrent. To be tuned to the correct wavelength, they can exploit a quantum well structure. Because of thermal effects that increase the temperature, they usually need cooling [58].

Graphene can improve this type of devices due to its high mobility with little temperature sensitivity: the former is useful in the thermal-based ones that usually have slow absorption response, while the latter can avoid the need of cooling in the thermal-based ones [59–64].

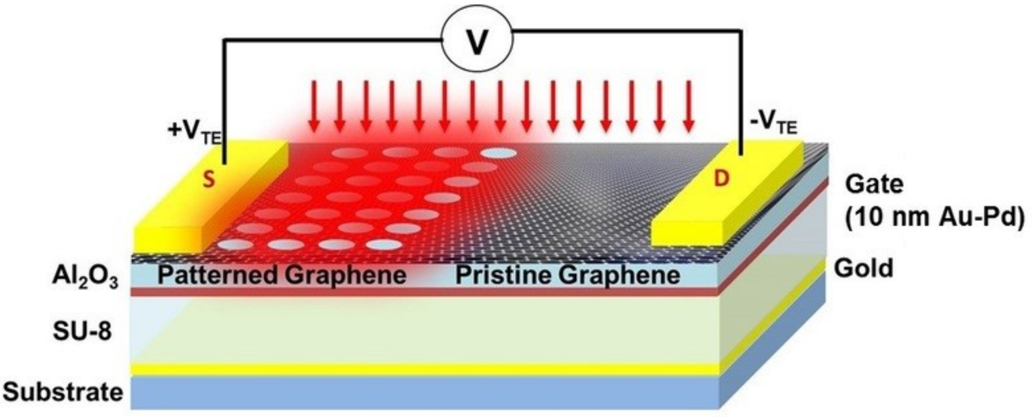

Figure 9 A tunable graphene-based mid-IR detector. (reprinted from [65])

2.2.4 Electrochemical sensors

Graphene has been used in electrochemical sensors due to its electrochemical potential, fast electron transfer rate and high redox peaks with linear cathodic and anodic currents [66].

Combined with redox enzymes via immobilization on the electrode surface has been used for direct electron transfer reactions thanks to its high detection capability [47].

It has been conjugated with many different materials to perform enzymatic reactions for glucose, cholesterol and hemoglobin sensors: Chitosan, nanoparticles, iron oxides, PVDF (polyvinylidene difluoride), nanofibers and nanocubes [67–79].

It has been used in the context of immunosensing, DNA sensing (Figure 10) and the detection of biomolecules like uric acid, ascorbic acid and dopamine, as well as hydrogen peroxide detector [80–87].

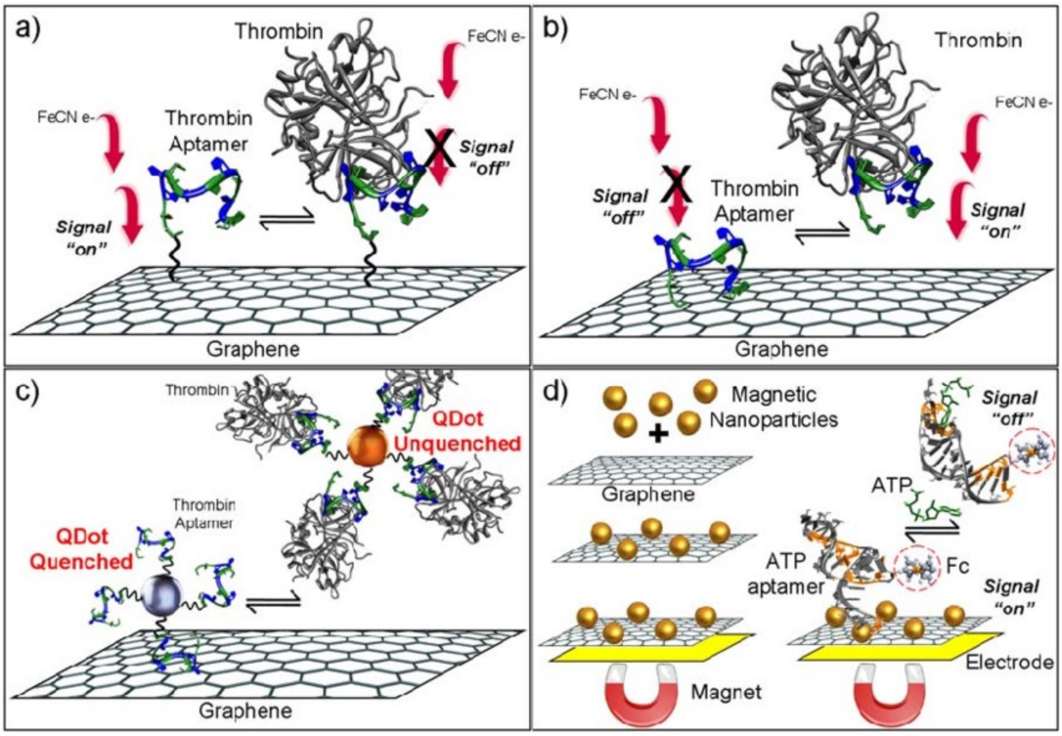

Figure 10 Different possible graphene-based electrochemical sensing platforms. Impedimetric sensors with (a) covalent and (b) non-covalent aptamer immobilization, (c) graphene quantum dots, (d) magnetic nanoparticles-graphene bioelectronics. (reprinted from [88])

2.2.5 Strain sensors

Graphene has proven to be a suitable material also for the fabrication of strain sensors because it generates a pseudo-magnetic field due to the shift in the Dirac cones and reduces the Fermi velocity [47]. This magnetic field can be implemented to determine the electronic structure change during strain.

The particular structure of graphene influences the response to strain: due to a different influence on the band gap, the relative strain results to be higher when parallel to the C-C bonds than when is perpendicular to them [47].

Researchers have worked with different polymer substrates under graphene in order to get a piezo-resistive effect for the strain detection, like polydimethylsiloxane (PDMS), Polyethylene terephthalate (PET) and Polyimide (PI) [89–91].

Graphene strain sensors were used as healthcare devices, as sound-signal acquisition and recognition devices and to detect human movements [92–101].

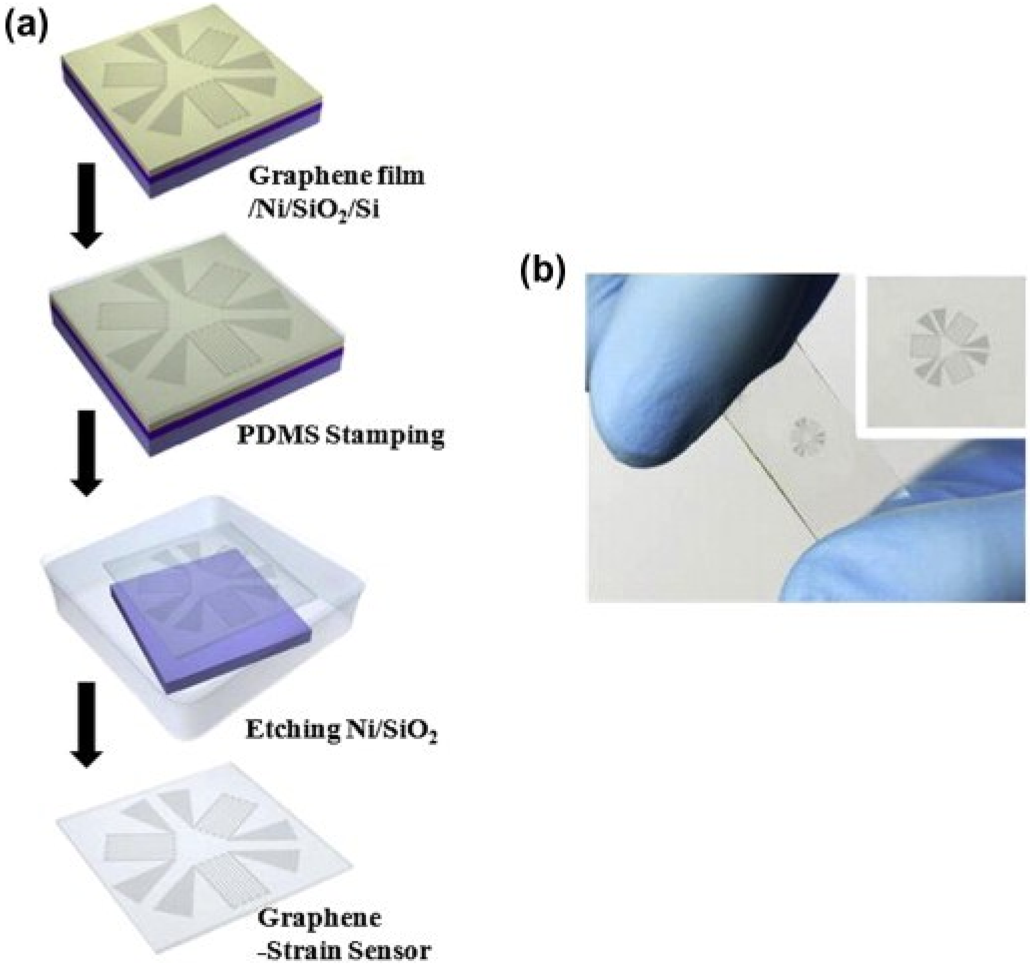

Figure 11 (a) Process steps and (b) final result of the fabrication of a transparent graphene strain sensor. (adapted from [102])

2.2.6 Electrical sensors

A lot of research has been performed on graphene-based electrical sensors for biomolecular, physical and chemical sensing.

G-FETs have been used for the detection of heavy metallic ions like cadmium, lead and mercury, going down to few nano molar ranges in detection. They have been able to detect also other ions like hydrogen, calcium and potassium. Other than ions, graphene-based electrical sensors have been able to detect gases like ammonia, nitrogen dioxide and other inorganic gases as well as to be used as pH sensors [103–116].

For the detection, G-FETs are usually functionalized specifically for the analyte that needs to be detected. Graphene can be used in different parts of the transistor, from the electrodes to the channel and the Gate, and can be functionalized itself.

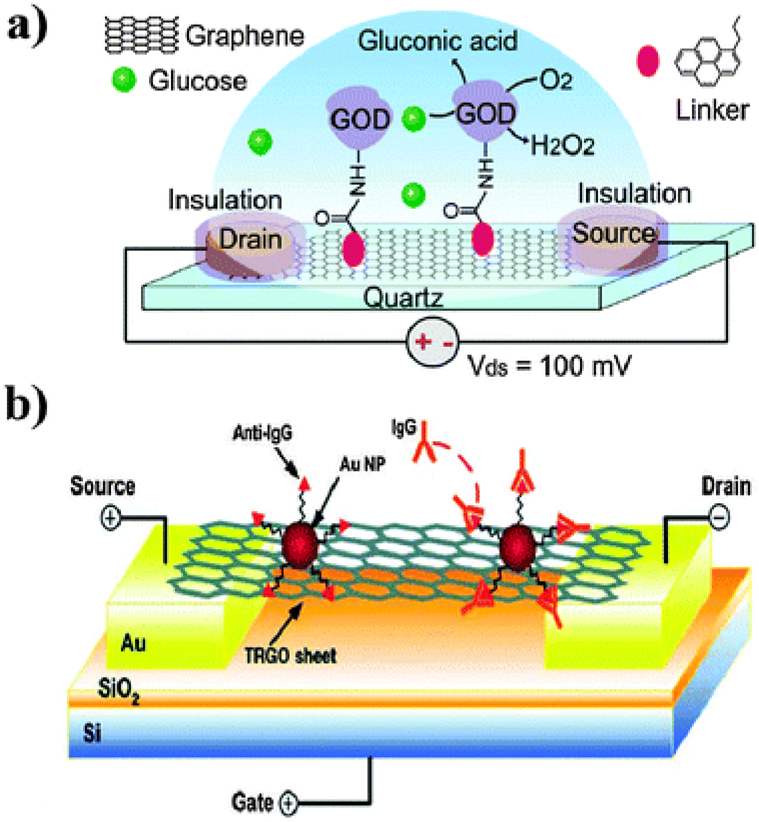

Figure 12 Two examples of graphene electrical sensors: (a) a glucose G-FET sensor and (b) an IgG G-FET sensor. (reprinted from [117])

2.3 Functionalization of graphene

An important role in the graphene studies resides in its functionalization: by understanding how different molecules can attach to the graphene structure and how this process affects its characteristics and behaviour is essential to open the road to several different applications.

In the following section the different ways of functionalizing graphene are portrayed, focusing on pristine graphene and the functionalizations that can be useful in the sensing field. The description is based on two reviews ([118,119]) and covers the functionalizations through covalent bonds, noncovalent bonds and nanoparticles.

2.3.1 Covalent bonds

Graphene functionalization by covalent bonds demonstrated to be useful for two main purposes: the dispersibility of graphene in organic solvents and the development of a bandgap [118,120].

In the first case, attaching organic groups to graphene allows dispersing it in compatible solvents, and this property is crucial in the preparation of nanocomposites.

In the second case, the functionalization with an organic functional group can often perturbate the electronic cloud due to the aromatic rings of graphene. This perturbation helps the formation of a bandgap, which can be extremely helpful in the exploitation of graphene for nanoelectronics [120].

In the case of pristine graphene the functionalization is possible only through the formation of a covalent bond by the reaction of the C=C bonds in the graphene structure and free radicals or dienophiles. For the free radicals, a diazonium salt is heated up until the free radical is produced and it attaches to the carbon atoms creating the covalent bond (Figure 13)[121,122].

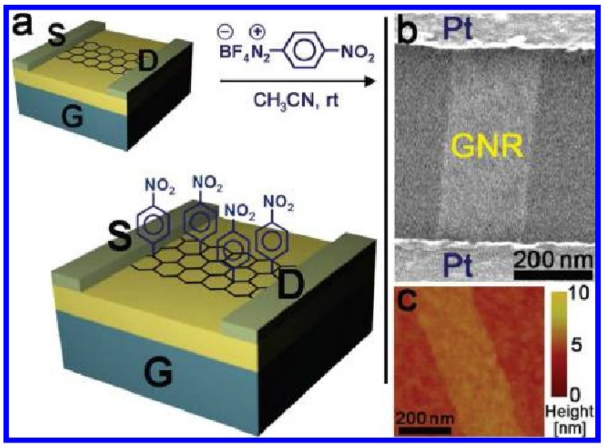

Figure 13 (a) An example of graphene functionalized by covalent bond with 4-nitrophenyl groups with its (b) SEM image and (c) AFM image. (adapted from [118])

Other than free radicals, also dienophiles can create a covalent bond with the sp^2 carbon atoms. From the carbon nanostructures known previously than graphene, one of the mostly used for functionalization was Azomethine ylide. This reacts with a 1,3 dipolar cycloaddition, which can result in several organic derivatives and open to a variety of different areas: polymer composites, biotechnology, nanoelectronic devices, drug delivery and solar cells [123–126].

2.3.2 Noncovalent bonds

The two main noncovalent bonds possible for the functionalization of graphene are van der Waals forces and π-π interactions. While van der Waals forces can be exploited in the case of organic molecules or polymers with high hydrophobic behavior, π-π bonds can be used for the functionalization in the case of molecules with highly delocalized electron system [119].

These interactions can be very useful in the application of graphene in many fields, since the bonds formed do not disrupt the π systems of the structure. For this reason, the graphene main characteristics like electrical conductivity are preserved, in contrast with the covalent interactions [127,128]. Moreover, noncovalent bonds have a mild and nonpermanent character which allows a safer treatment of the final functionalized product.

The π bond can have three conformations, depending on the molecules configuration and the electron cloud: face-to-face, slipped and edge to face (Figure 14a). In the case of graphene, it is possible to have a face-to-face or an edge-to-face bond depending on the position where it forms: while in the center only face-to-face bonds will form, on the edge of the structure there is a small possibility that an edge-to-face bond occurs due to a hydrogen atom which terminates the structure (Figure 14b)[119].

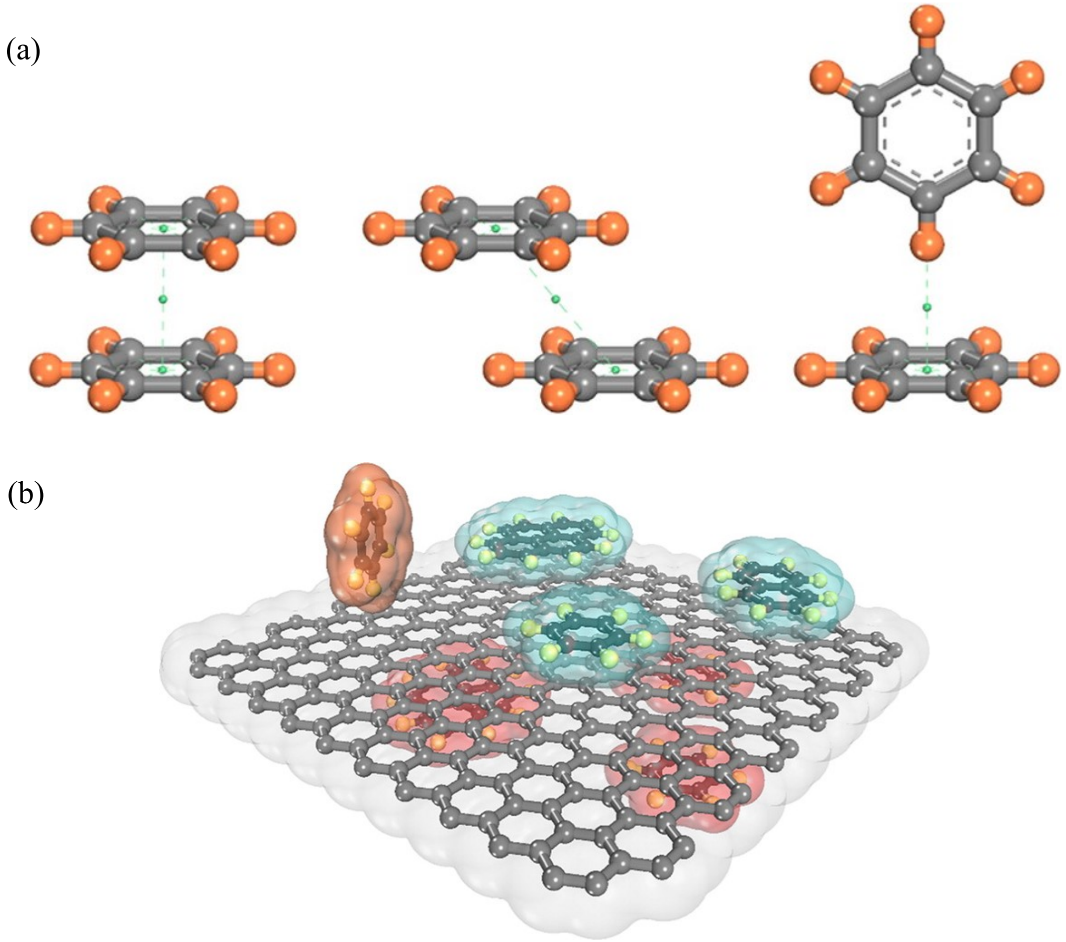

Figure 14 (a) The three possible π-π bonds conformations: face-to-face (left), slipped (middle) and edge-to-face (right). (b) An example of possible π-π interactions from benzene, naphthalene, or pyrene molecules above and below the graphene structure. (adapted from [119])

3 Chapter

Materials and methodologies

The work here described has been partially previously published in [129–131]. In the following, the materials and methodologies for the device preparation processes and the functionalization study are presented. At the beginning of each paragraph a short contextualization is present to outline the background from which the work started.

3.1 Graphene Devices

The idea started from the previous know-how present in the research group: the expertise on standard lithographic processes and device fabrication was combined with the experience in microfluidics fabrication techniques and polymeric materials knowledge.

For this reason, at first G-FETs (Graphene Field-Effect Transistors) were fabricated through lithography and standard PMMA-assisted graphene transfer process and tested. Then, a new transfer process was tested and optimized in order to be compared with the previous one. The aim was to achieve a device with comparable behavior to the reference one, but with the improvement of an easier, less operator-dependent and also more scalable process.

Once reached a certain standard and repeatability in the process, it was used to fabricate different devices with the help of the expertise of a visiting PhD student from the State Key Laboratory for Manufacturing System Engineering, Xi’an Jiaotong University in China. The new transfer process had major advantages in the fabrication of graphene Schottky diodes.

3.1.1 G-FETs made by PMMA Transfer

3.1.1.1 Fabrication process design

The basic motivation was to have a transistor which could be used as a sensor. To this aim, the configuration which could guarantee the best results was thought to be the EGOFET (Electrolyte Gated Organic Field Effect Transistor). By being electrolyte gated, the analyte to be detected could be inserted in the liquid interposed between the gate and the active material (graphene in our case).

From the biologist perspective, the only device related request was to be small enough to fit easily in the multi-well plates for the functionalization, but big enough to be easily handled.

As a consequence, the device layout was based on a 10x10 mm^2 single chip footprint; the channel was 20 μm wide and 2 mm long (Figure 15a). The electrodes were made in gold to ensure optimal conductivity. In order to have graphene only between the electrodes and to avoid unwanted currents, a patterning step was added.

For the passivation, a Polyimide resist was used: this way it could be directly patterned by lithography without any etching or lift-off step; moreover, it was way better for the other transfer method in which the substrate was flexible. This way the comparison between the two would have been more reliable.

Finally, a PDMS chamber was developed to contain the liquid electrolyte only on a small area, the one covering the channel. This way the gate could be inserted from the top in the electrolyte. The PDMS was chosen for its biocompatibility and for a possible straightforward future integration of a microfluidic device (Figure 15b).

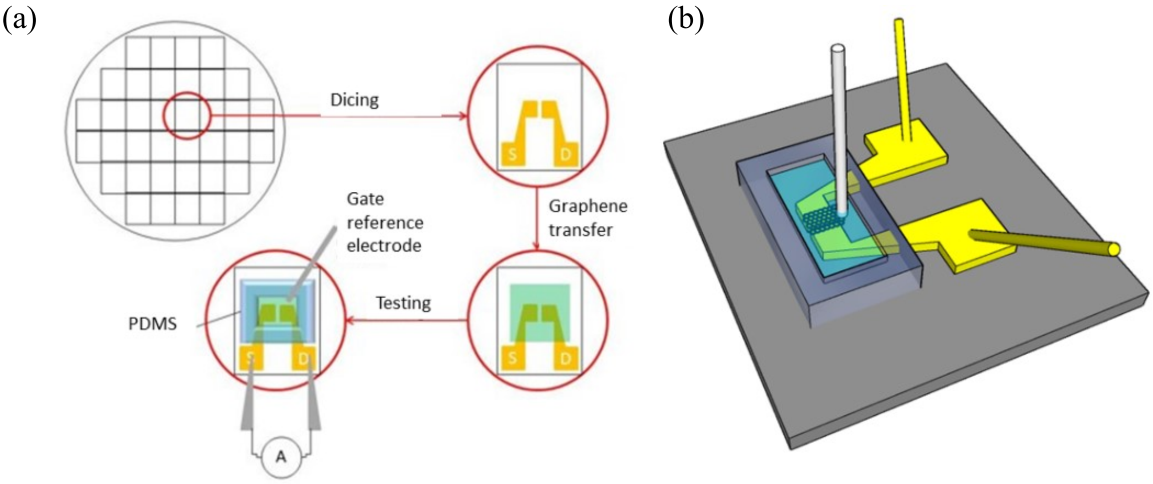

Figure 15 (a) The layout of the device, from the initial wafer to the final chip. (b) Final design of the device: the yellow gold electrodes, the transparent PDMS chamber and graphene in between the channel.

To allow comparison with the transfer process described in “3.1.2 G-FETs made by Hot Embossing Transfer”, the same transfer will be performed on a COC (Cyclo-Olefin-Copolymer) substrate.

3.1.1.2 Materials

Materials were chosen according to the requested performances. When possible, the purest materials were used, allowing to avoid possible contaminations.

COC foils 140 μm thick TOPAS 8007×04 were provided by Tekni-plex.

Cu foils 25 μm thick for the graphene growth were purchased from GoodFellows.

HCl (37%) for the Cu cleaning, Anisole for PMMA solution, Acetone, Ethanol and 2-Propanol (all ACS grade or better) for the washings and rinsings were all purchased from Sigma-Aldrich.

$FeCl_3$ solution for Cu removal was purchased from Nuova Delta Elettronica.

PMMA was purchased from Sigma Aldrich.

4” Silicon wafers (500 ± 25 μm) with 1 μm oxide layer were purchased from NanoVision for the isolated substrate.

For the lithography AZ1518 positive resist was purchased from Microchemicals.

Gold etchant was custom made from Iodine and Potassium Iodide purchased from Carlo Erba.

Titanium etchant was custom made from Hydrofluoric acid 39% (Carlo Erba), Hydrogen Peroxide 30% (Sigma Aldrich) and DI water.

The PDMS and curing agent for the containment chamber was purchased from Sylgard.

Polyimide photoresist AM 271 was purchased from Asahi Kasei.

3.1.1.3 Fabrication

The first step was the patterning of the electrodes for the Source and Drain of the G-FETs.

The masks for all the lithographic steps were patterned with the LW405 Laser Writer from Microtech onto purchased Soda Lime masks coated with 500 nm of AZ1518 resist.

The selected substrates were 4” Si/SiO_2 wafers and COC foils for the comparison, on which 100 nm of Au were evaporated with 10 nm of Ti working as adhesion layer (Figure 16a). The substrate was then spin coated with the AZ1518 positive photoresist and exposed to UV with the Neutronix Quintel NXQ-4006 Mask Aligner following the recipe recommended by the provider (Figure 16b).

After the development of the resist, the substrate was wet etched with the Gold Etching and Titanium Etching solutions (Figure 16c). Every chip was composed of two electrodes separated by the channel as described in the section “3.1.1.1 Fabrication process design”.

Cu foils 2 x 2 cm^2 were rinsed in HCl solution (HCl 37% in H_2O 1:3) to remove the native oxide. After that, graphene was grown on them by a Moorfield NanoCVD 8G with the standard recipe provided by default with the machine: after 2 minutes at 900 °C with Argon and Hydrogen, the chamber is heated to 1000 °C and Methane is injected to start the nucleation and allow the monolayer growth. Then 10 minutes with only Argon and Hydrogen at without heating end the recipe.

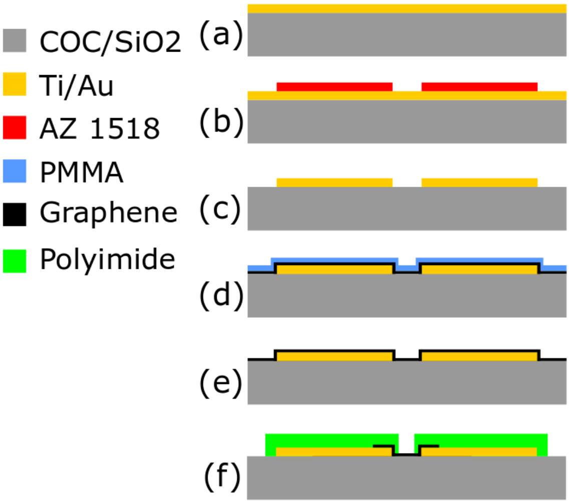

Figure 16 Device fabrication process: (a) metal deposition, (b) lithography, (c) electrodes patterning, (d) graphene transfer, (e) PMMA removal, (f) graphene patterning and passivation.

Then a layer of PMMA (solution 1.35% in anisole) was carefully spin coated on the top side of the Cu which holds the graphene. The Cu foil was carefully masked on the sides to avoid any infiltration of the PMMA under the foil, which would ruin the whole process by preventing the Cu etching.

The sample was then dipped in a $FeCl_3$ solution for copper removal. After that, two rinsing cycles in DI water allowed to remove the $FeCl_3$ excess. The graphene/PMMA foil obtained was then placed onto the previously patterned substrate with the electrodes and dried under vacuum to allow a better PMMA removal (Figure 16d).

The samples were then rinsed three times in Acetone to completely remove the PMMA and to leave the electrodes covered by the graphene (Figure 16e).

Another lithographic step with the AZ1518 was performed to pattern graphene only in correspondence of the channel between the electrodes. Then an etching step was performed by oxygen plasma for 30 s to remove the graphene everywhere except than in the channel.

Finally, another lithographic step allowed to pattern the Polyimide resist (Asahi Kasei AM271) in order to passivate the devices (Figure 16f) (spinning at 4000 rpm for 60 s, final thickness of ≈2 μm).

3.1.1.4 Raman characterization

As usually recognized for graphene, to have an evaluation of its quality a Raman spectroscopy was performed with a Renishaw inVia Raman microscope equipped with a Leica DMLM microscope with a 50x objective.

The source used for the excitation of the substrate was a 514.5 nm solid state laser with a nominal output power of 100 mW and a 10% filter. For every spectrum 5 accumulations were taken with 2 s exposure. The laser spot was defocused in order to decrease the laser power density at the sample and avoid photodegradation.

To allow comparisons between the spectra, they were normalized with respect to the laser power.

3.1.1.5 Electrical characterization

A Keysight B2912A Source/Measure unit (Figure 17b) combined with a probe station was used to perform the electrical measurements. A PDMS chamber with a capacity of 50 µl was placed on the active area of the transistor to contain the solution for the tests.

An Ag/AgCl leak free reference electrode was used as the gate and was directly placed in the chamber with the solution (Figure 17a).

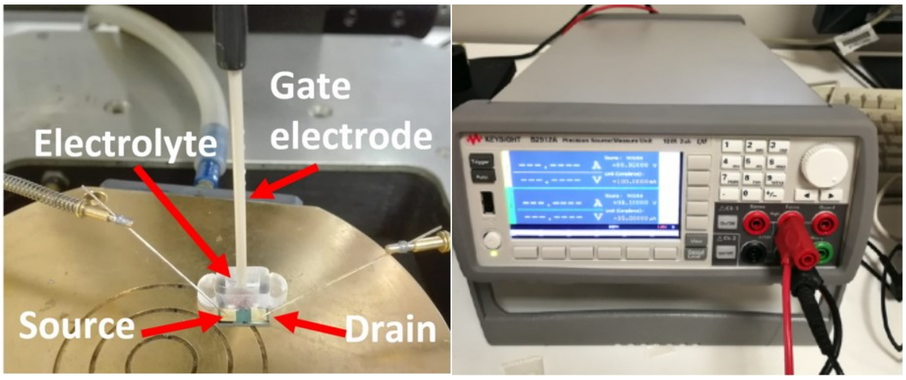

Figure 17 (a) Characterization setup (close-up view of the device under test in the probe station) and (b) Keysight B2912A Source/Measure unit.

For the measures two voltage sweeps were performed: one continuous for the gate between -1 V to +1 V and the other for the drain at constant values (20 mV, 70 mV, 120 mV, 170 mV and 220 mV). They were performed in DI water and used to obtain the device trans-characteristics (drain current vs gate voltage).

The absence of leakage through the gate was carefully checked by measuring in parallel the leakage current, which compared with the drain current always showed a difference of at least 4 orders of magnitude.

3.1.1.6 AFM characterization

A Bruker Atomic Force Microscope in tapping mode was employed for the AFM characterization with probes with elastic constant of 40 N/m and nominal resonance frequency of 300 kHz.

3.1.1.7 pH sensing tests

The pH sensing behavior of G-FETs with Si/SiO_2 as a substrate was then studied. Phosphate Buffered Saline (PBS 1x, Sigma Aldrich) at physiological concentration was used as the electrolyte solution. This buffer was chosen to investigate a pH range and ionic strength that can be useful in the biomedical field. Small amounts of HCl or NaOH were added to the initial solution with pH 7.4 to obtain buffers with pH from 6.4 to 8.2. A VWR SB70B pH-meter was used to measure the pH values before performing the sensing experiments.

3.1.2 G-FETs made by Hot Embossing Transfer

3.1.2.1 Fabrication process design

In this case, the motivation was to improve the process described in "3.1.1.3 Fabrication". The graphene transfer process is extremely operator dependent and takes a lot of time to be performed, moreover with little margin to be up-scaled at the industrial level. An alternative easy approach to transfer graphene was then conceived, relying on the exploitation of polymers characteristics and microfluidics know-how.

If graphene can be imprinted in a polymer and form a bond with it strong enough to keep them together also after rinses with solvents and lithographic steps, the most critical and time-consuming step of the process could be improved a lot.

A polymer material well known in microfluidics for its resistance to solvents, its transparency and flexibility, is COC (Cyclo Olefin Copolymer) that was thus evaluated as to be a valid candidate for the substrate (Figure 18).

In order to have a process where the parameters can be tuned easily and with high precision and good reproducibility, the imprinting step was performed through a Hot Embossing equipment: the instrument is commonly used to bond polymers or to emboss master samples into polymers and can apply controlled force and heat, giving the process the needed repeatability.

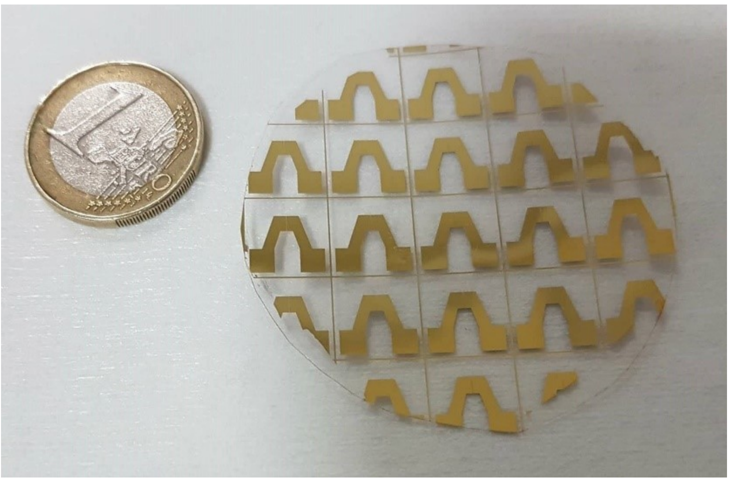

Figure 18 Device layout on a 2" wafer-like COC substrate.

In this way, after the graphene growth via CVD, the Cu foil could be directly embossed into the polymer on which the electrodes have been previously patterned. After the Cu etching, if the bond with graphene is strong enough, it will remain onto the sample, allowing the process to continue as previously described.

The embossing process needs to be optimized in order to allow the Cu foil to remain attached to the COC also during the handling of the sample.

The other design requests were the same as before: so the final design was an EGOFET 10 x 10 mm^2 with a channel 20 μm wide and 2 mm long, provided with Au electrodes, Polyimide for passivation and a PDMS chamber.

3.1.2.2 Materials

Materials were chosen according to the requested performances. Whenever possible, the purest materials were used, allowing to avoid possible contaminations.

COC foils 140 µm thick TOPAS 8007×04 were purchased from Tekni-plex.

Cu foils 25 µm thick for the graphene growth were purchased from GoodFellows.

HCl (37%) for the Cu cleaning, Anisole for PMMA solution, Acetone, Ethanol and 2-Propanol (all ACS grade or better) for the washings and rinsings were all purchased from Sigma-Aldrich.

$FeCl_3$ solution for Cu removal was purchased from Nuova Delta Elettronica.

For the lithography AZ1518 positive resist was purchased from Microchemicals.

Gold etchant was custom made from Iodine and Potassium Iodide purchased from Carlo Erba.

Titanium etchant was custom made from Hydrofluoric acid 39% (Carlo Erba), Hydrogen Peroxide 30% (Sigma Aldrich) and DI water.

The PDMS and curing agent for the containment chamber was purchased from Sylgard.

Polyimide photoresist AM 271 was purchased from Asahi Kasei.

3.1.2.3 Fabrication

Also in this case the first step was the patterning of the Source and Drain electrodes on the substrate. The masks for all the lithographic steps were patterned through the LW405 Laser Writer from Microtech onto purchased Soda Lime masks coated with 500 nm of AZ1518 resist.

The substrate chosen was a COC foil, which was cut in 4” circles to fit the instruments that usually work with wafers. On the COC 100 nm of Au were evaporated with 10 nm of Ti working as adhesion layer (Figure 19a). Later on, also Au deposition alone was tested, and the adhesion proved to be the same, so in some cases was used without Ti.

The wafer was then spin coated with the AZ1518 positive photoresist and exposed to UV with the Neutronix Quintel NXQ-4006 Mask Aligner. Due to the very low T_g of the COC (78 °C), some modifications to the recipe were made: the temperature for the soft bake needed to be no more than 75 °C, so the bake time was increased to 5 min (Figure 19b). After the development of the resist, the foil was wet etched with the Gold Etching and Titanium Etching solutions (Figure 19c). Every chip was composed of two electrodes separated by the channel as described in the section “3.1.2.1 Fabrication process design”.

Cu foils 2 x 2 cm^2 were rinsed in HCl solution (HCl 37% in H_2O 1:3) to remove the native oxide. After that, graphene was grown on them with a Moorfield NanoCVD 8G with the standard recipe provided by default with the machine and previously reported.

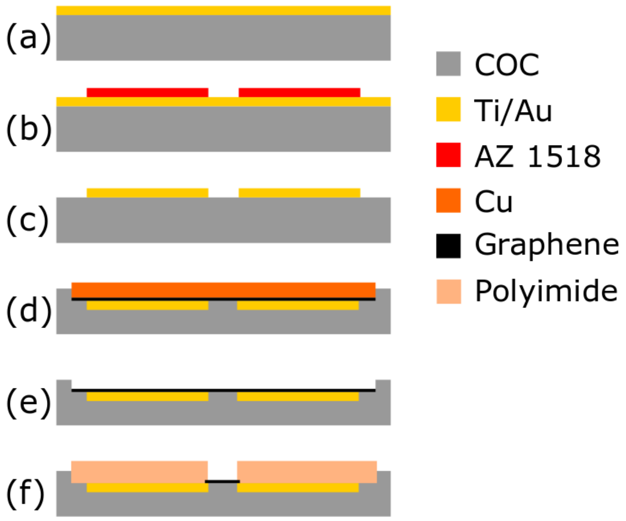

Figure 19 Device fabrication process: (a) metal deposition, (b) lithography, (c) electrodes patterning, (d) graphene embossing, (e) Cu removal and (f) graphene patterning and passivation.

The Cu foil with graphene was then embossed through the Hot Embossing HEX01 JENOPTIK Mikrotechnik on the COC foil (Figure 19d). After some tests, it was found that the Cu foil needed to cover completely the electrodes: if the side of the Cu foil remained on an electrode during the embossing, being the thickness of the Cu foil much higher than the thickness of the electrodes, the embossing process would break the electrode interrupting the electrical continuity for the measures.

To allow a safer handling of the samples and avoid the attaching of the COC to the embossing plates, two Si wafer were used between the embossing plates and the samples.

Due to the T_g of the COC (78 °C) and to ensure the best contact with the graphene, the samples were embossed at 80° C with an applied force of 10000 N for 120 s.

To remove the Cu a wet etching step was performed with a $FeCl_3$ solution for 20 min. $FeCl_3$ residues were removed by thoroughly rinsing the samples first in DI water and then in HCl solution (Figure 19e).

Another lithographic step with the AZ1518 was performed to pattern graphene only in correspondence of the channel between the electrodes. Then an etching step was performed with oxygen plasma for 30 s to remove the graphene everywhere except than in the channel.

Finally, another lithographic step allowed to pattern the Asahi Kasei AM271 Polyimide resist in order to passivate the devices (Figure 19f) (spinning at 4000 rpm for 60 s, final thickness of ≈2 µm).

3.1.2.4 Raman characterization

To get an evaluation of graphene quality a Raman spectroscopy was performed with a Renishaw inVia Raman microscope equipped with a Leica DMLM microscope with a 50x objective.

The source used for the excitation of the substrate was a 514.5 nm solid state laser with a nominal output power of 100 mW and a 10% filter. For every spectrum 5 accumulations were taken with 2 s exposure. The laser spot was defocused in order to decrease the laser power density at the sample and avoid photodegradation.

To obtain the graphene spectrum, also the COC alone was characterized by Raman spectroscopy. Both spectra (graphene on COC and COC alone) were normalized with respect to the laser power and then subtracted to obtain the graphene contribution without the COC interference. This way the spectrum obtained could be compared with the other spectra.

3.1.2.5 Electrical characterization

A Keysight B2912A Source/Measure unit (Figure 17b) combined with a probe station was used to perform the electrical measurements. A PDMS chamber with a capacity of 50 µl was placed on the active area of the transistor to contain the solution for the tests.

An Ag/AgCl leak free reference electrode was used as the gate and was directly placed in the chamber with the solution (Figure 17a).

For the measures two voltage sweeps were performed: one continuous for the gate between -1 V to +1 V and the other for the drain at constant values (20 mV, 70 mV, 120 mV, 170 mV and 220 mV). They were performed in DI water and used to obtain the device trans-characteristics (drain current vs gate voltage).

The absence of leakage through the gate was carefully checked by measuring in parallel the leakage current, which compared with the drain current always showed a difference of at least 4 orders of magnitude.

The G-FETs made via hot embossing were then tested as flexible devices: the devices were folded with a curvature radius of 8 mm by pulling the electrodes upwards while forcing the channel down. Measurements were taken as described before.

3.1.2.6 AFM characterization

A Bruker Atomic Force Microscope in tapping mode was employed for the AFM characterization with probes with elastic constant of 40 N/m and nominal resonance frequency of 300 kHz.

3.1.2.7 pH sensing tests

The pH sensing behavior of G-FETs fabricated via hot embossing on COC was then studied. Phosphate Buffered Saline (PBS 1x, Sigma Aldrich) at physiological concentration was used as the electrolyte solution. This buffer was chosen to investigate a pH range and ionic strength that can be useful in the biomedical field.

Small amounts of HCl or NaOH were added to the initial solution with pH 7.4 to obtain buffers with pH from 6.4 to 8.2. A VWR SB70B pH-meter was used to measure the pH values before performing the sensing experiments.

3.1.2.8 Electrical response to bending tests

The G-FETs made via hot embossing were then tested as flexible devices: the devices were folded with a curvature radius of 8 mm by pulling the electrodes upwards while forcing the channel down (Figure 20), and measurements were taken as described in “3.1.2.5 Electrical characterization”.

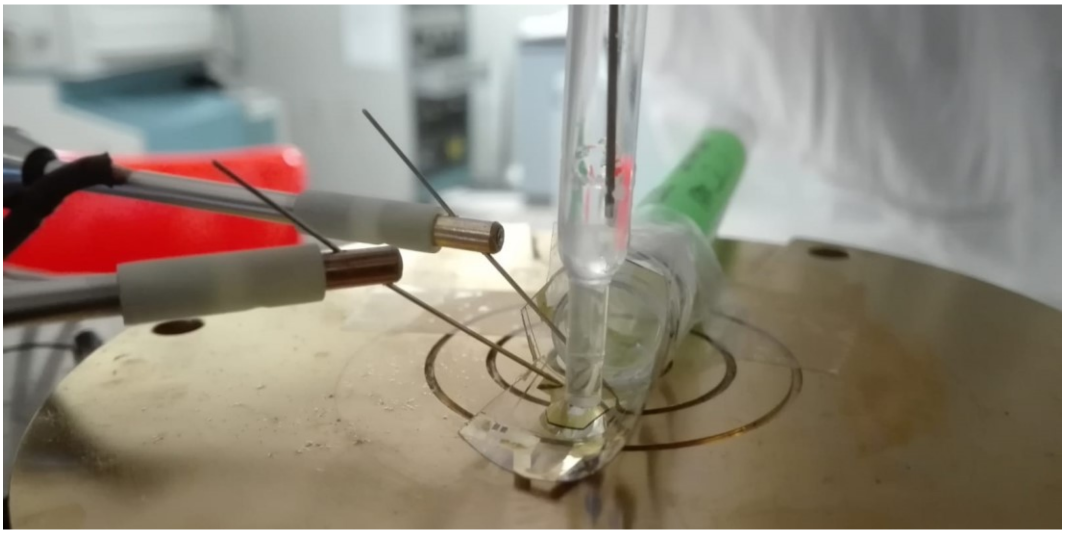

Figure 20 Measurement setup for the electrical characterization under bending.

3.1.3 Graphene Schottky Diode

3.1.3.1 Fabrication process design

After having optimized the new transfer process, next step was to find the implementation that could get the best out of it. Considering the characteristics of the COC, the decision turned towards optics: its transparency allowed the photons to pass through it without influencing graphene behavior.

In this field the graphene/Silicon Schottky junction is one of the most important graphene based photosensitive devices. In Gr/Si Schottky photodiodes electron-hole pairs are excited by the silicon absorption of the photons that arrives from the light source and pass through the graphene. In the process, the photo-generated carriers are collected by graphene which provides a high-speed pathway for carrier transport.

In this case, the new transfer method could give even one more advantage to the fabrication process. After the first Hot Embossing assisted transfer, the COC foil could be embossed again on the Silicon sample.

When transferring the graphene onto the Silicon to form the junction, the COC remains on top of the samples, providing a package that protects the device while does not interact with the incident photons.

3.1.3.2 Materials

Materials were chosen according to the requested performances. Whenever possible, the purest materials were used, allowing to avoid possible contaminations.

COC foils 140 µm thick TOPAS 8007×04 were purchased from Tekni-plex.

Cu foils 25 µm thick for the graphene growth were purchased from GoodFellows.

HCl (37%) for the Cu cleaning, Acetone, Ethanol and 2-Propanol (all ACS grade or better) for the washings and rinsings were all purchased from Sigma-Aldrich.

$FeCl_3$ solution for Cu removal was purchased from Nuova Delta Elettronica.

For the lithography AZ1518 positive resist was purchased from Microchemicals.

Gold etchant was custom made from Iodine and Potassium Iodide purchased from Carlo Erba.

Titanium etchant was custom made from Hydrofluoric acid 39% (Carlo Erba), Hydrogen Peroxide 30% (Sigma Aldrich) and DI water.

BOE solution (7:1) was purchased from Microchemicals.

4” Silicon wafers (500 ± 25 µm) with 1 µm oxide layer on one side and Ti/Au layer on the other side were provided by State Key Laboratory for Manufacturing System Engineering, Xi’an Jiaotong University, China.

3.1.3.3 Fabrication

Cu foils 2 x 2 cm^2 were rinsed in HCl solution (HCl 37% in H_2O 1:3) to remove the native oxide. After that, graphene was grown on them by a Moorfield NanoCVD 8G with the standard recipe provided by default with the machine and previously reported.

To allow a safer handling of the samples and avoid the attaching of the COC to the embossing plates, two Si wafers were used between the embossing plates and the samples.

Due to the T_g of the COC (78 °C) and to ensure the best contact with the graphene, the samples were embossed at 80 °C with an applied force of 10000 N for 120 s.

To remove the Cu a wet etching step was performed with a $FeCl_3$ solution for 20 min. $FeCl_3$ residues were removed by thoroughly rinsing the samples first in DI water and then in HCl solution.

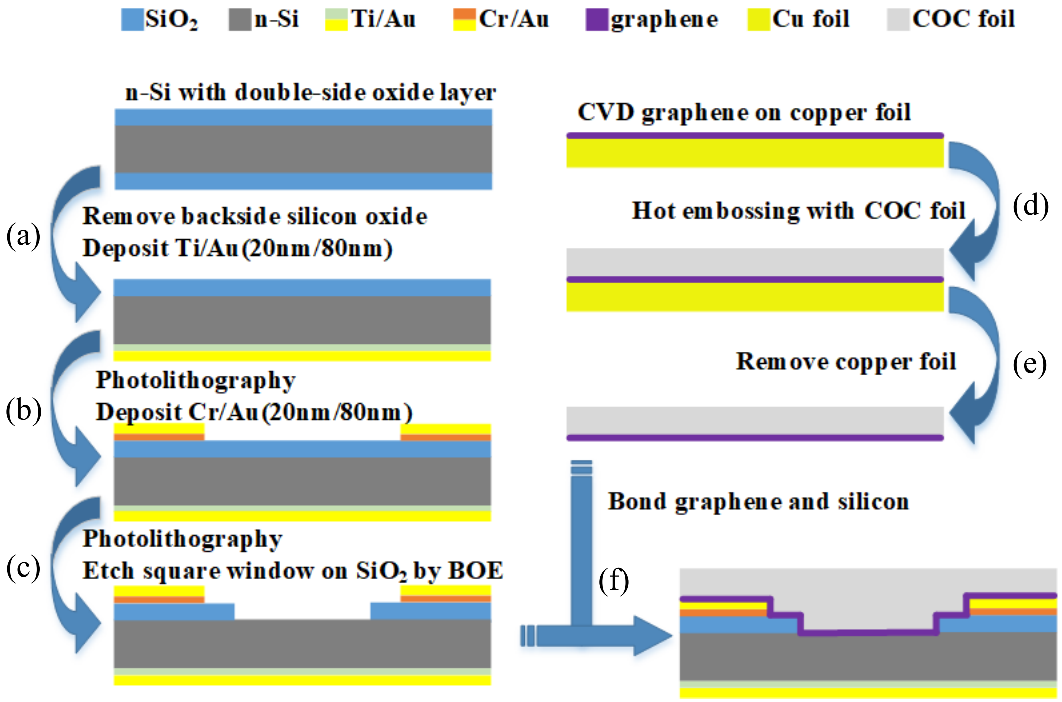

Figure 21 Device fabrication process: (a) back-side silicon oxide removal and metal deposition, (b) top-side metal deposition and photolithography for electrodes patterning, (c) photolithography and etching for SiO_2 removal, (d) graphene growth and embossing, (e) Cu removal, (f) final embossing

For the Schottky junction fabrication the substrate chosen was an n-type Si wafer with 300 nm SiO_2. First, the backside SiO_2 layer was wet etched by HF, and an ohmic contact was obtained by the deposition of Ti/Au (20 nm/80 nm) through e-beam evaporation (Figure 21a). After that, on the front side of the SiO_2/Si wafer electrodes were patterned and evaporated with Cr/Au (20 nm/80 nm)(Figure 21b).

These first steps were performed at the State Key Laboratory for Manufacturing System Engineering, Xi’an Jiaotong University, China, which provided directly the processed wafer.

A square window (1.6 × 1.6 mm^2) was defined through photolithography on the top side of the substrate, followed by the removal of the SiO_2 layer through a wet etching step in buffered oxide etch (BOE) solution (Figure 21c). Then the Schottky contact was formed in the window by a second hot embossing step that bonded graphene with the samples previously described, defining the active area of the photodetector.

3.1.3.4 Raman characterization

A Reflex InVia Raman microscope (Renishaw plc, Wotton-under-Edge, UK) with a 514.5 nm solid state laser with a nominal output power of 100 mW and a 10% filter was used for the characterization of the hot-embossing-transferred graphene. For every spectrum 5 accumulations were taken with 2 s exposure. The laser spot was defocused in order to decrease the laser power density at the sample and avoid photodegradation.

To obtain the graphene spectrum, also the COC alone was characterized by Raman spectroscopy. Both spectra (graphene on COC and COC alone) were normalized with respect to the laser power and then subtracted to obtain the graphene contribution without the COC interference. This way the spectrum obtained could be compared with the other spectra.

3.1.3.5 Electrical and photoelectrical characterization

Electrical characterizations were carried out with a Keysight B2912A Source/Measure unit, while photoelectrical characterizations were performed with a semiconductor laser under dark and 633 nm illumination. A Sanwa LP-1 was used for the laser power calibration before the measurements (Figure 22).

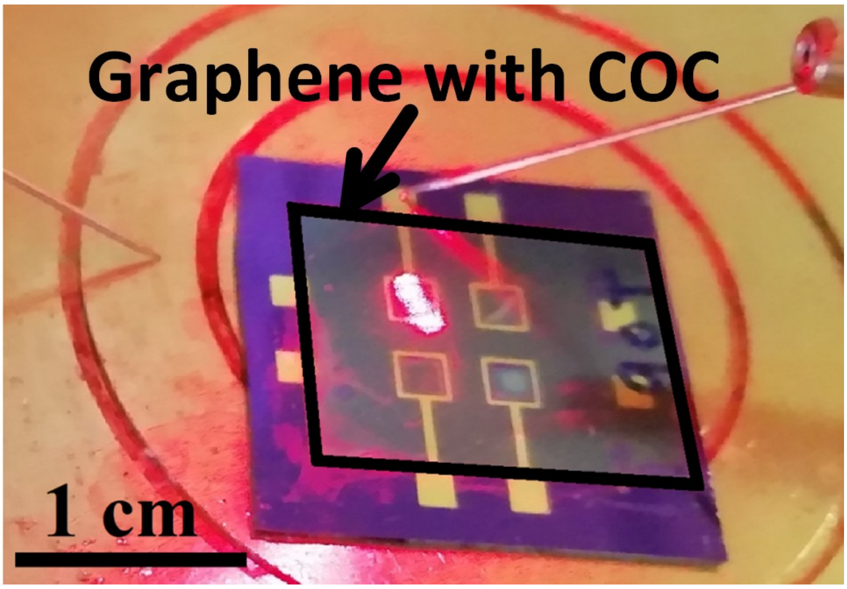

Figure 22 Final device under test with laser.

The behavior of Gr/Si Schottky diodes was evaluated extracting the ideality factor and Schottky barrier height from the current-voltage curve following the thermionic emission theory.

3.2 Graphene Functionalization

The main focus of a sensor is the detection. Because of that, one of the main part of the sensor is the one that allows specific capturing the target molecule. This is particularly relevant for biosensing and it can be performed by either the gate or the channel. While the functionalization of gold is very well known and established in the literature, with standard protocols, the case of graphene is different.

Graphene functionalization has not been studied as thoroughly as gold functionalization, and there is plenty of room for its understanding and optimization.

If optimized, its functionalization could not only give new perspectives in the sensor industry, but also in chemistry and physics.

3.2.1 Protocol and study design

The problem with graphene functionalization is that we need to create a link between the specific capture probe of the sensor (usually a protein receptor such as an Antibody or an oligonucleotide probe) and the graphene. In order to do so, a functional group needs to be exposed, like a COOH or an Amine group.

Due to the chemistry of graphene, the usual methods to functionalize it are covalent bonds or π-π stacking. Covalent bonds require harsh reactions, while π-π stacking can be performed in milder conditions which should allow avoiding possible graphene or sensor changes in behavior. In fact for covalent bonds defects in graphene structure are formed, since a π bond needs to be broken to change the ibridation of some C atoms from sp^2 to sp^3, while in π-π stacking there is only an interaction between the electronic clouds [118,119]. For this reason π-π stacking process was chosen. The functionalization molecule will then need π bonds and a functional group that can bond with the capture probe.

The general idea was then to find few molecules that showed these two characteristics and analyze how they interact with graphene by Raman spectroscopy. All of these molecules should have an extended delocalized electron system thanks to the presence of one or more aromatic ring in their structures to allow a π-π stacking interaction. Usually the surface of graphene is functionalized with harmful polycyclic aromatic hydrocarbons. In this study, we tried to focus our attention on less hazardous molecules.

The first step was to test the molecules and characterize them through Raman spectroscopy under dry and in solution conditions, in order to get a first idea of their vibrational pattern. A first selection was then made based on the solubility of the molecule, the compatibility of the solvents with the fabrication processes and the overlap between the molecules' Raman bands and the spectrum of graphene.

One molecule was chosen afterwards to perform the tests required for the definition of the protocol steps. The substrate chosen for graphene in the study was first Silicon and then it was switched to gold to avoid interferences in the spectra, that could be detrimental during the optimization phase.

A Raman spectrum was taken from graphene alone, to compare it with the following steps.

The first step was the incubation, and different times and different concentrations of the molecules were investigated to assess the better parameters. After that, another spectrum was taken.

Then two washing steps were performed, one with ethanol to remove the molecule in excess and one with PBS to understand how the interaction between the molecule and graphene was affected by a typical buffer used for biomolecules. After every wash a Raman characterization was performed.

For the data analysis three parameters were taken into account: since the objective is to obtain only a monolayer attached to the graphene, the full spectrum of the molecule will not be strong enough, except for some molecules featured by very high Raman cross sections. For this reason, only differences in the graphene peaks before and after the incubation will be considered. The parameters checked were then width, intensity and position of the three graphene bands (D, G, 2D). Also the peak intensities ratio (which reflects the quality of graphene) I_D/I_G and I_{2D}/I_G were considered.

After a first protocol has been established, other molecules were analyzed to find the most suitable one for the functionalization purpose.

3.2.2 Study steps

3.2.2.1 Raman characterization

Raman spectroscopy was performed with a Renishaw inVia Reflex Raman microscope equipped with a Leica DMLM microscope with a 50x or a 5x objective. The source used for the excitation was a 514.5 nm solid state laser with an output power of 100 mW.

3.2.2.2 Molecule selection

A first list of 21 molecules was screened with Raman spectroscopy in their dry state:

1. Trans-cinnamic acid
2. Caffeic acid
3. Trans-ferulic acid
4. Azure A chloride
5. Sinapic acid
6. L-Triptophan
7. Toluidine Blue O (TBO)
8. Indole-3-butyric acid
9. Tryptamine
10. Cumarine SH
11. Cumarine SS
12. Benzophenone COOH
13. Benzophenone maleimide
14. Cinnamic acid alkyne
15. Cinnamic acid maleimide
16. Benzophenone alkyne
17. Benzophenone amine
18. Pyrene
19. Protoporhyrin
20. Tionine acetate
21. Ferulic acid alkyne

After this, a first selection was made based on the quality of the spectra obtained and on their solubility in ethanol or water.

A second characterization was then performed on the molecule in solution for:

1. Caffeic acid (in ethanol) (Figure 23a)

2. Tionine acetate (in water) (Figure 23b)
3. Triptophane (in water) (Figure 23c)
4. Trans-cinnamic acid (in ethanol) (Figure 23d)
5. Indole-3-butyric acid (in ethanol) (Figure 23e)
6. Protoporphyrin (in ethanol) (Figure 23f)
7. Pyrene (in ethanol) (Figure 23g)
8. Benzophenone COOH (in ethanol) (Figure 23h)

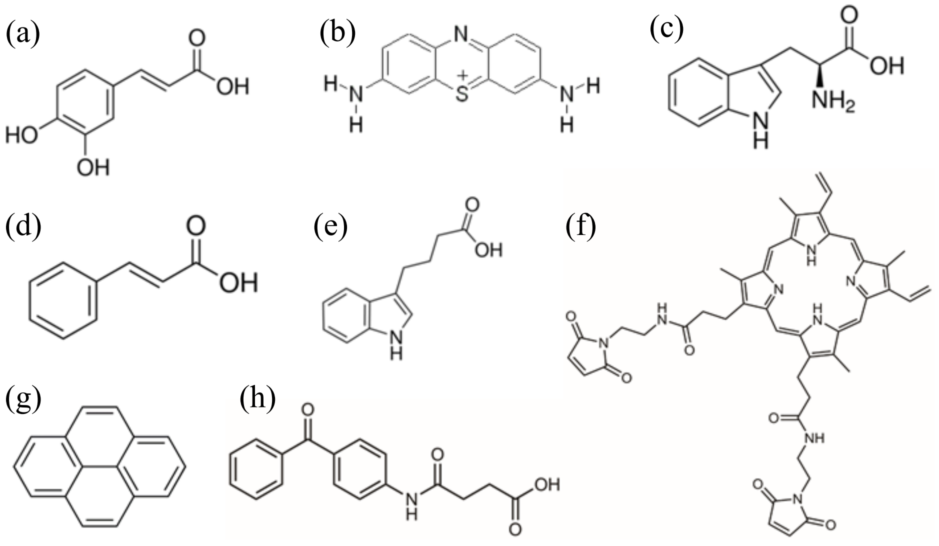

Figure 23 Molecules for the study: (a) Caffeic acid, (b) Tionine acetate, (c) Triptophane, (d) Trans-cinnamic acid, (e) Indole-3-butyric acid, (f) Protoporphyrin, (g) Pyrene, (h) Benzophenone COOH.

The molecule selected for the thorough analysis was the Caffeic acid due to its good solubility in ethanol and its spectrum which does not overlap too much with the graphene one.

3.2.2.3 Graphene transfer

Cu foils 2 x 2 cm^2 were rinsed in HCl solution (HCl 37% in H_2O 1:3) for native oxide removal. Graphene was then grown on them with a Moorfield NanoCVD 8G with the standard recipe provided by default with the machine.

Then a layer of PMMA (solution 1.35% in anisole) was carefully spin coated on the top side of the Cu which holds the graphene. The Cu foil was carefully masked on the sides to avoid any infiltration of the PMMA under the foil, which would ruin the whole process by preventing the Cu etching.

The sample was then laid in a $FeCl_3$ solution for copper removal. After that, two rinsing passages in DI water allowed removing the $FeCl_3$ excess. The graphene/PMMA foil obtained was then placed onto the substrate (Silicon at first, then Gold evaporated on Silicon) and dried under vacuum to allow a better PMMA removal.

The samples were then rinsed three times in acetone to completely remove the PMMA.

3.2.2.4 Protocol definition

First graphene spectra were taken. A first large area map was acquired with the 5x objective to check the sample for regions with a non-complete graphene coverage and exclude them from the next spectroscopic analysis. Then two Raman maps were taken for each sample in two different spectral windows at low (250-2000 cm^{-1}) and high (2250-3750 cm^{-1}) Raman shifts and the 50x objective. A map consists of a points grid where for every point a Raman spectrum is acquired. For the first map 60 points with a distance of 300 μm were defined, while in the second case 60 points with 10 μm between them were acquired. The acquisition parameters were chosen to be 2 seconds as exposure time for 5 accumulations and 10% of the output laser power. A defocus of 10% was used.

At first, three different concentrations, 1, 10 and 100 mM of Caffeic acid solution in ethanol, were tested. At the same time, two different incubation times, overnight and 1 h, were tested. For every sample, the spectra were taken with the same parameters as for graphene only. Afterwards, a 5 minutes rinse in ethanol was used to remove the excess of caffeic acid and another Raman analysis was performed. A final PBS rinse of 5 minutes and final Raman spectra were taken.

After the first performed analysis, that will be discussed in “4.3.2 Protocol definition” section, the incubation time was set at 1 h and the concentration at 10 mM and the following tests were performed under such conditions.

The other molecules were then tested following this protocol and the results compared with the ones for Caffeic acid.

3.2.2.5 Data analysis

All the spectra were analyzed through the instrument software Wire 3.4. At first the possible presence of cosmic rays was checked with the Cosmic Ray Remover and the unwanted peaks removed. Then, the three chosen parameters (Intensity, Width, Position) were found for every main peak of graphene, so G, D and 2D using the fitting tool of the software. The analysis was then extended with R Studio. The parameters obtained for each spectrum of the Raman map were then averaged and compared between the steps. An averaged spectrum was also obtained.

4 Chapter

Results and discussion

In this chapter the results are displayed and discussed. Obtained data, graphs and tables are shown and explained, with the interpretation of the behavior of the devices and graphene.

4.1 G-FETs

The different devices (PMMA transfer on Silicon, PMMA transfer on COC and Hot Embossing transfer on COC) were compared in their performances and regarding the quality of graphene.

The devices made via PMMA transfer on COC were made to be able to consider also the interaction of the substrate in the analysis and eliminate the possibility that the differences between the transfer methods (either in positive or in negative) were influenced by the selected substrate instead of the transfer method used.

The following sections will discuss the comparison of the graphene Raman spectra, of the trans-characteristics of the devices, their transconductances, Dirac points, pH sensing and the COC behavior as flexible sensor.

4.1.1 Raman spectra

The first fundamental result in the Hot Embossing transfer was the preservation of the graphene also under the high molding pressure used during the transfer (25 MPa), which was firstly demonstrated by the conduction between the electrodes and then confirmed by the Raman spectrum (Figure 24a).

To obtain this, any residual mechanical stress on the COC was avoided thanks to the low process temperature and time selected. Moreover, the graphene covered the whole area of the device, inducing a negligible polymer chains re-arrangement and avoiding the possibility of defects arising from the transfer, as it can be assessed from the corresponding Raman spectrum.

The Raman spectrum of the graphene embossed on the COC showed 3 main peaks: the D peak at 1343 cm^{-1}, the G one at 1572 cm^{-1} and the 2D at 2678 cm^{-1}, while the I_{2D}/I_G ratio was 1,94 (Figure 24a). The G band is due to the in-plane vibration of the carbon-carbon bonds of the graphitic layers, the D only arises in the presence of defects which disrupt the symmetry of the sp^2 systems and the 2D correspond to the second order modes of the D [132]. The monolayer condition of graphene is demonstrated by the ratio and the form of the 2D and G peaks, while a small D peak confirmed that the planar structure present only few defects.[133,134]

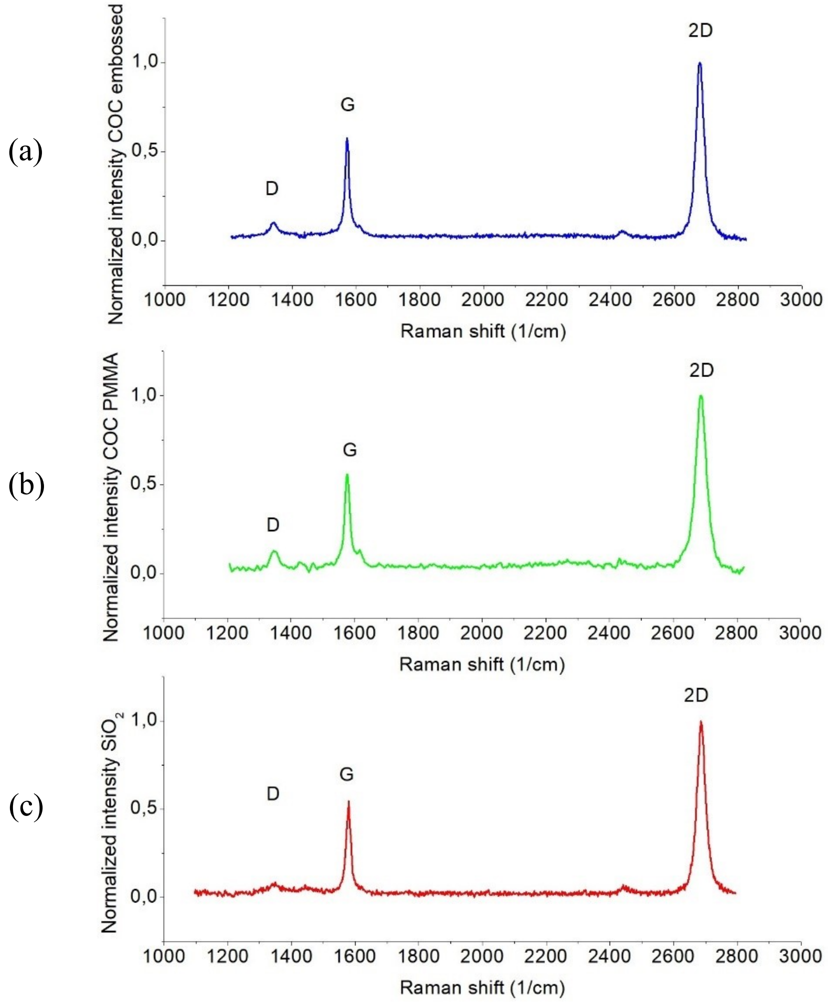

Figure 24 Raman spectra comparison between (a) graphene embossed on COC, (b) graphene PMMA-transferred onto COC and (c) graphene PMMA-transferred onto SiO_2.

The comparison with the others showed that the same peaks can be found in the graphene PMMA transferred on COC Raman spectrum (D at 1346 cm^{-1}, G at 1576 cm^{-1} and 2D at 2687 cm^{-1}) (Figure 24b) and in the one transferred on SiO_2/Si (D at 1340 cm^{-1}, G at 1576 cm^{-1} and 2D at 2671 cm^{-1}) (Figure 24c). The three spectra showed a comparable ratio between 2D and G peaks. A slightly higher D peak can be seen for the COC PMMA-transferred, which means that more defects could be present, but no big differences are shown. [133,134]

To sum up, the cleaner spectrum remains the one on SiO_2, but the embossed one demonstrated to be very similar, and the D peak on the PMMA-transferred on COC means that the problem could be due to the flexibility of the COC during the transfer.

The embossing transfer method anyway demonstrated to be better than the PMMA mediated one when comparing the same substrate, and almost identical to the standard PMMA mediated transfer on Silicon.

4.1.2 AFM characterization

An AFM analysis was performed in order to get more information on the graphene on COC (Figure 25): graphene covers the non-planar surface of the COC which shows valleys and hills of few tens of nm.

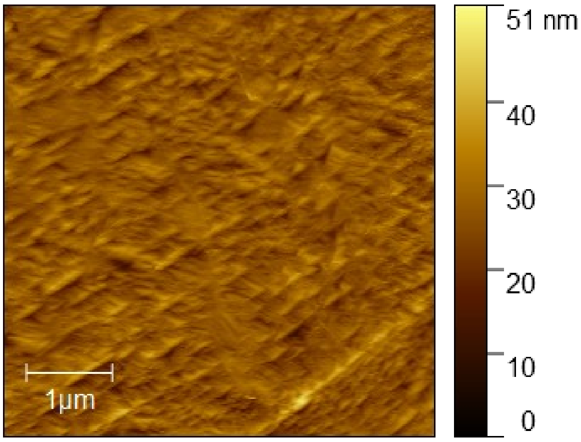

Figure 25 Sample of Hot-Embossing-transferred graphene on COC characterized by AFM.

This could be the cause of the D peak in the Raman spectrum and of the differences in mobilities with respect to SiO_2/Si substrate.

4.1.3 Electrical characterization

4.1.3.1 I_{ds} v V_g Trans-characteristic

The electrolyte-gated G-FETs fabricated via hot embossing showed the classical ambipolar characteristics: the trans-characteristic has the typical V-shape and the samples changes from p to n-type (Figure 26a).

(a)

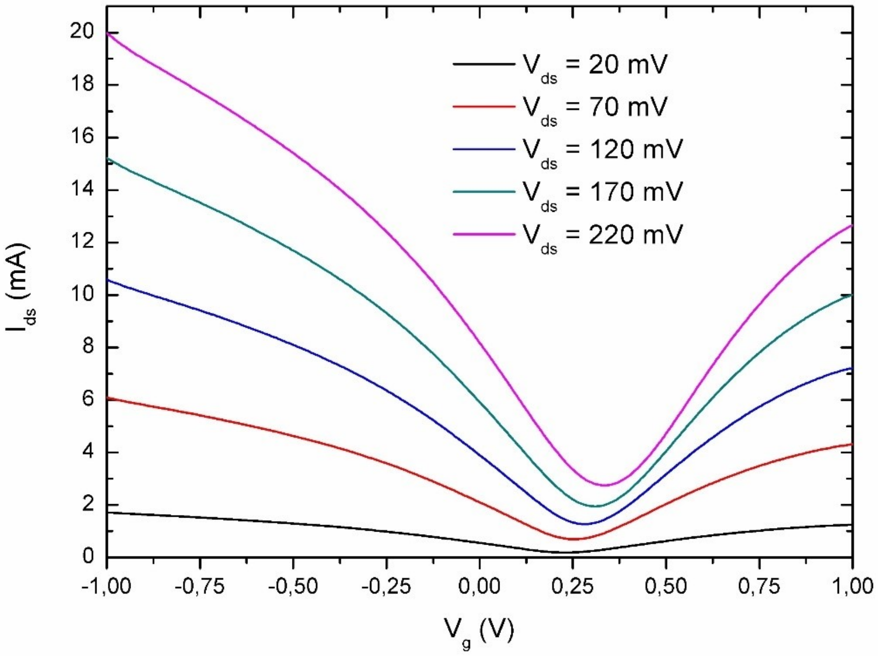

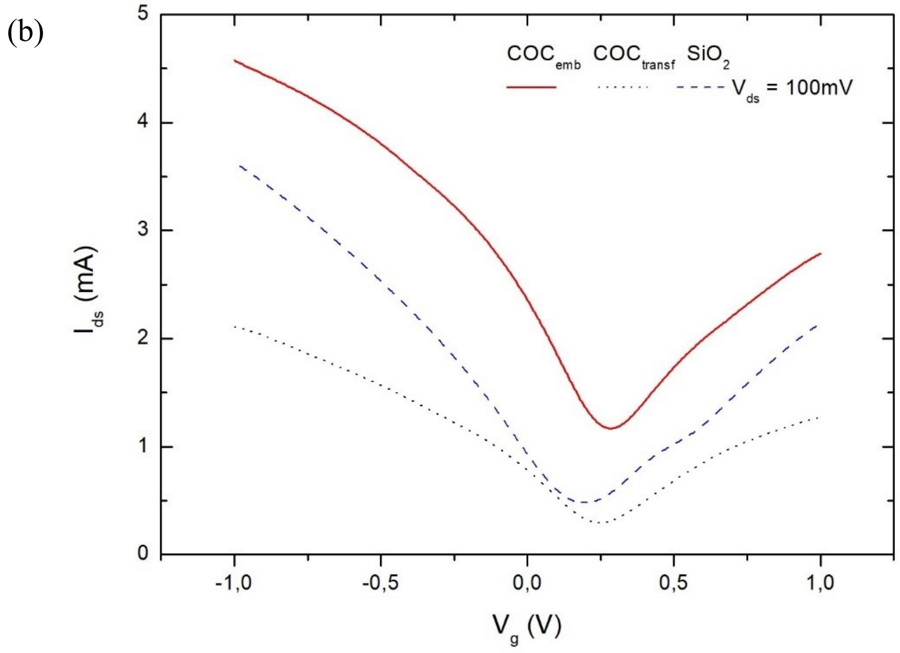

Figure 26 (a) Trans-characteristics at different V_{ds} in DI water of G-FET fabricated via hot embossing. (b) Comparison between the trans-characteristics of G-FET fabricated via PMMA assisted transfer on Si/SiO_2 and COC and via hot embossing on COC in DI water at fixed drain voltage.

The shift in the Dirac points (that will be discussed in “4.1.3.2 Dirac points and transconductances”) means that the V-shape is not centered at 0 V. For this reason, the steeper parts of the curve (both left and right) are not centered as well, with the right one between 0.4 and 0.7 V and the left one between -0.1 and 0.2 V.

Being the left one also the steeper between the two (as it can also be seen more clearly in Figure 26b), this situation can be useful: since for the sensing purpose the best starting point is the one with the steeper trans-characteristic (due to the fact that a small voltage variation creates a bigger current shift), fixing the V_g between 0 and 0.1 V allows operating in the steepest point with the advantage of consuming less.

No significant charging effects can be found since the Dirac point of the three devices (PMMA-assisted transfer on COC and on Si/SiO_2 and via hot embossing on COC) have no substantial differences (Figure 26b).

The COC transferred one shows the worst behavior: it has the lowest conduction and the less steep shape, which means that it is the least useful to be used as a sensor.

The embossed COC and the SiO_2 show a similar shape, with the embossed one that is slightly steeper near the Dirac point. The difference resides in the conduction, with the embossed COC showing a shift of around 1 mA almost everywhere.

This results in a higher consumption which can be a disadvantage, but on the other side can allow an easier detection of the current shift during sensing, which is the main purpose of the device.

4.1.3.2 Dirac points and transconductances

The substrate is probably responsible of the charging effect which causes the shift from the 0 V of the Dirac points, as in the case of SiO_2[135]. The use of electrolytic delamination could improve the shift of the Dirac points by avoiding possible contaminations raising from copper etching[136].

No significant charging effects can be found, since the Dirac point of the G-FETs transferred with PMMA on COC results to be similar to the one transferred on Si/SiO_2 (Figure 27b). However, the transferring process with PMMA on COC causes some problems due to the flexibility of the substrate: possible fractures in the graphene structure could reduce the overall final conductance and the maximum trans-conductance (Figure 27a).

The Dirac point of graphene embossed on COC demonstrates to be comparable to the PMMA transferred one on both substrates (COC and Si/SiO_2) (Figure 27b), bearing in mind also that considering the error bars almost the whole area is overlapped.

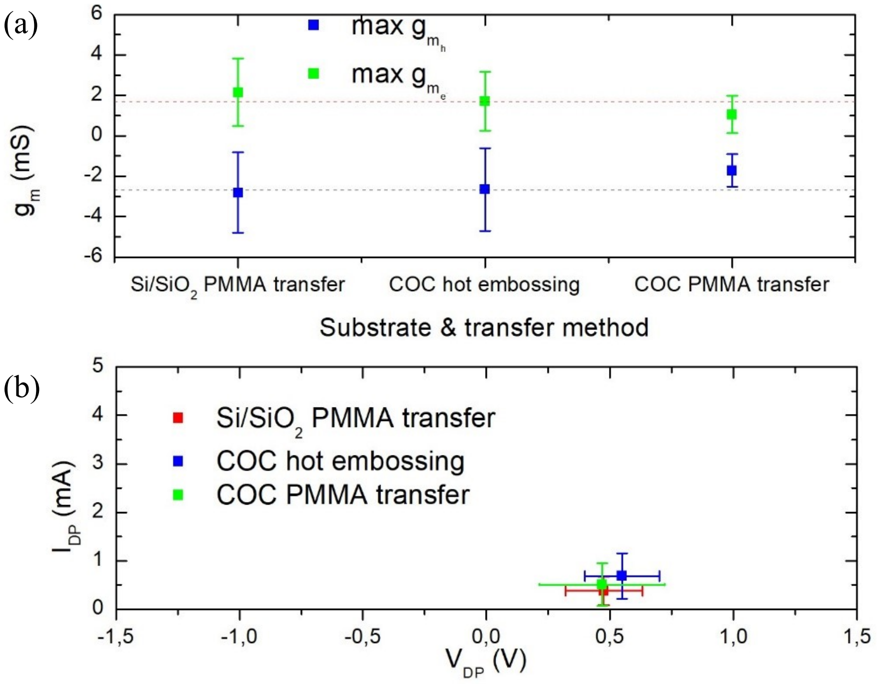

Figure 27 (a) Comparison between the maximum hole transconductance (g_{mh}) and electron transconductance (g_{me}) for the three different processes at V_{ds} = 100 mV; (b) Comparison between the Dirac voltage V_{DP} and Dirac current I_{DP} for the three different processes at fixed V_{ds} = 100 mV

The embossed graphene trans-conductance results to be higher than the PMMA-transferred graphene on COC, and similar to the PMMA-transferred one on Si/SiO_2 (Figure 27a). Even the error bars are comparable, meaning that the reproducibility is very similar in both embossed COC and Si/SiO_2.

The calculations of the charge carriers field effect mobilities where performed as [137]:

$$\mu_{e/h} = \frac{g_{m_{e/h}} L}{V_{ds} W C_{TG}} \qquad (1)$$

Where C_{TG} is the top gate capacitance and corresponds to the series connection of the EDL capacitance ($C_{EDL} \simeq 18\ \mu F \cdot cm^{-2}$)[138] and graphene quantum capacitance ($C_Q \simeq 2\ \mu F \cdot cm^{-2}$)[139]. The obtained $\mu_{e/h}$ are shown in Table 1.

Device	G_{m_e}(mS)	G_{m_h}(mS)	$\mu_e\left(\frac{cm^2}{V \cdot s}\right)$	$\mu_h\left(\frac{cm^2}{V \cdot s}\right)$
COC_{emb}	1.70	2.67	141	221
COC_{transf}	1.05	1.72	87	142
SiO_2/Si	2.15	2.81	178	233

Table 1 Transconductances ($G_{m_{e/h}}$) and field effect mobilities ($\mu_{e/h}$) calculated from the transfer characteristics for both electron and holes.

The COC PMMA-mediated transfer demonstrates to be the one with the worst characteristics due to its lower conductance and transconductance. The problem probably resides in the transfer difficulty, which is due to the flexibility of the substrate that increase the possibility to fracture the graphene structure.

The embossed COC shows a decrease of 20% in electrons transconductance and mobility and a decrease of 5% in hole transconductance and mobility. With respect to the PMMA-mediated transfer on Si/SiO_2, still being the best one, the difference is minimal also considering the possibility to further optimize the embossing transfer.

4.1.4 Sensing behavior

4.1.4.1 pH sensing

pH sensing experiments have been performed in a buffer with high ionic strength (PBS 1x, ionic strength ≃ 162.7 mM) with the PMMA transferred on Si/SiO_2 G-FET and the COC-embossed G-FET, since they showed the highest transconductances.

pH variation in the range 6.4-8.2 was successfully detected by both devices, with a variation detection as low as $\Delta pH = 0.2$ (Figure 28). The pH range has been chosen in order to remain within the buffering range of PBS (pH 5.8 - 8.0).[140]

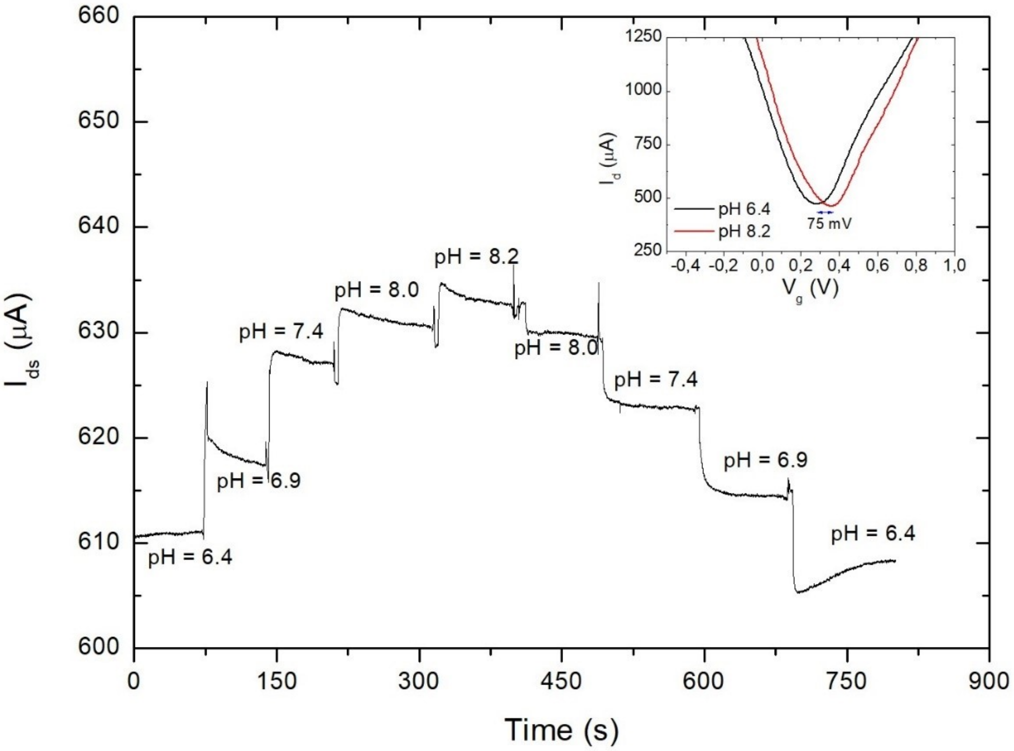

Figure 28 pH sensing behavior of G-FET fabricated via hot embossing on COC. Measurements were performed at high ionic strength (PBS 1x used as pH buffer). Inset: trans-characteristic shift arising from a pH variation from 6.4 to 8.2.

A change in the buffer could allow exploring a wider pH range. The peaks and valleys that can be seen at the beginning and at the end of each pH value are due to the perturbation produced by the removal of the previous solution and the addition of the following one.

The different currents for the same pH values that can be seen between the first half and the second half of the graph derive from the current drift of the device. The same effect can be seen in each part with the same pH, where the current slowly decreases. The drift may be due to different effects: for example, it can derive from the intrinsic drift of the gate electrode, or could arise from the adsorption of the buffer ions in the active layer. This effect can be avoided with a long stabilization time or with a calibration time that allows to extract a drift line which can be subtracted from the data.

Figure 29 shows the calibration curves obtained for both devices. The comparison between the calibration curves shows that COC-embossed G-FET performances are similar to PMMA transferred G-FET on Si/SiO_2 ones, since the difference is only 1.5% of the I_{pH}/I_0.

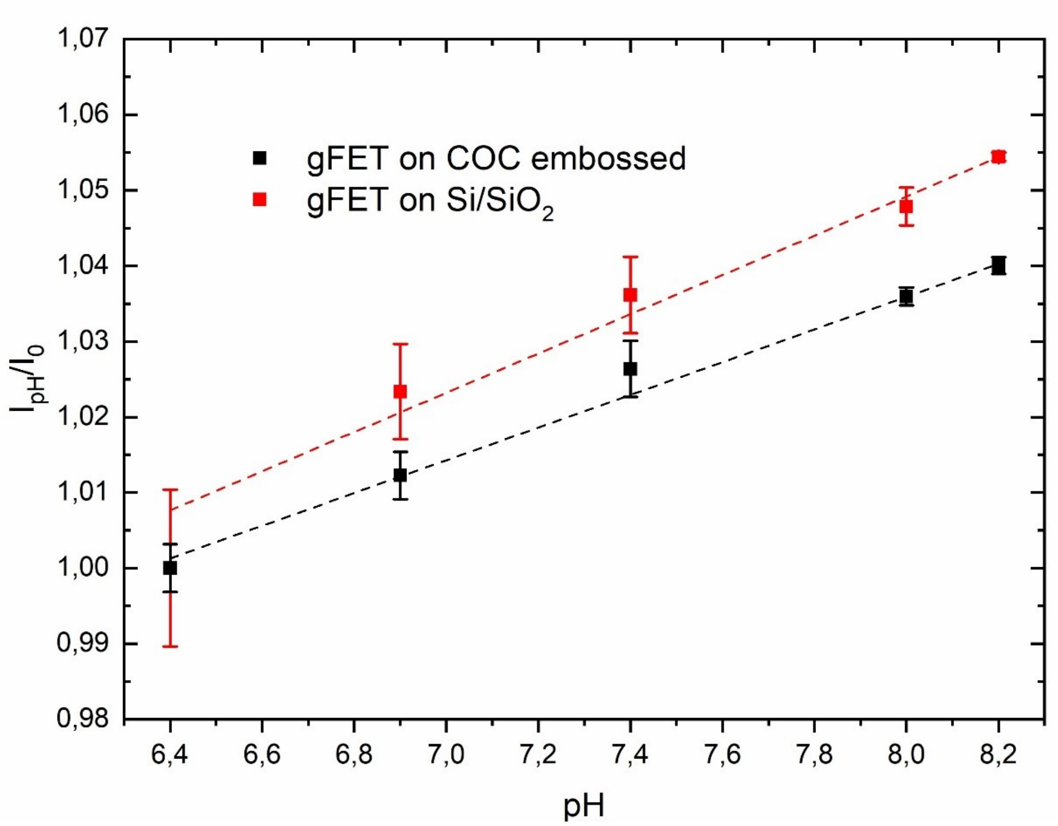

Figure 29 Comparison between pH calibration curves obtained from G-FET fabricated via hot embossing on COC and via PMMA transfer on Si/SiO$_2$. A current normalization with respect to the value at pH 6.4 has been performed in order to allow the comparison between the two devices.

The pH sensitivity S obtained from the shift of V_{DP} for the PMMA transferred on Si/SiO$_2$ G-FET ($S_{Si} \simeq 28$ mV/pH) is comparable to values found in the literature [141] and is 50% lower than the one calculated for the COC-embossed G-FET ($S_{COC} \simeq 42$ mV/pH). This shows that the embossed COC device demonstrates to be a good candidate for sensing purposes.

4.1.4.2 Flex sensor

G-FETs fabricated via hot embossing were tested as devices for flexible electronics: their performances were compared between flat and bent positions. As showed in Figure 30, the device common V-shaped characteristic is still present, demonstrating similar performances between the flat position and the bent position.

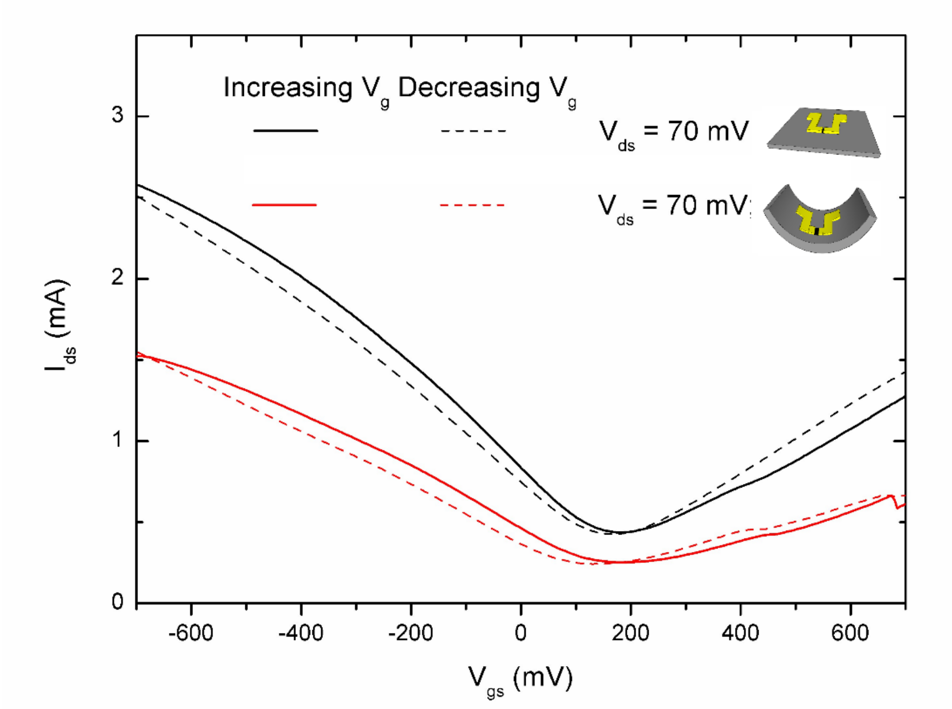

Figure 30 Trans-characteristics comparison between the same device in flat position (black) and bent position (red) with V_{ds}=70 mV.

The current decrease does not influence critically the device performances, showing that the device could be used for flexible electronics due to its good electric behavior under stress and as flex sensor due to its sensibility to bending.

4.2 Schottky diode

The results here described were obtained thanks to the collaboration of the PhD student Yiming Wang from State Key Laboratory for Manufacturing System Engineering, Xi'an Jiaotong University in China.

In the following part, the quality of the Schottky diode made by Hot Embossing transfer process of graphene is discussed. The photocurrent response under different incident light surface power densities and their time dependence were analyzed and compared with the models and the previously published works.

4.2.1 Raman characterization

Graphene transferred by hot embossing on the COC substrate shows a Raman spectrum (Figure 31) with the characteristics three main graphene peaks: D peak at 1346 cm^{-1}, G peak at 1582 cm^{-1}, and 2D peak at 2678 cm^{-1}. The 2D peak shows a sharp and symmetric shape, with a full width at half maximum of 35 cm^{-1}, and an intensity ratio with respect to the G peak of 1.75. The monolayer nature of the graphene is demonstrated by the shape of the peaks and the intensity ratio.[142–144]

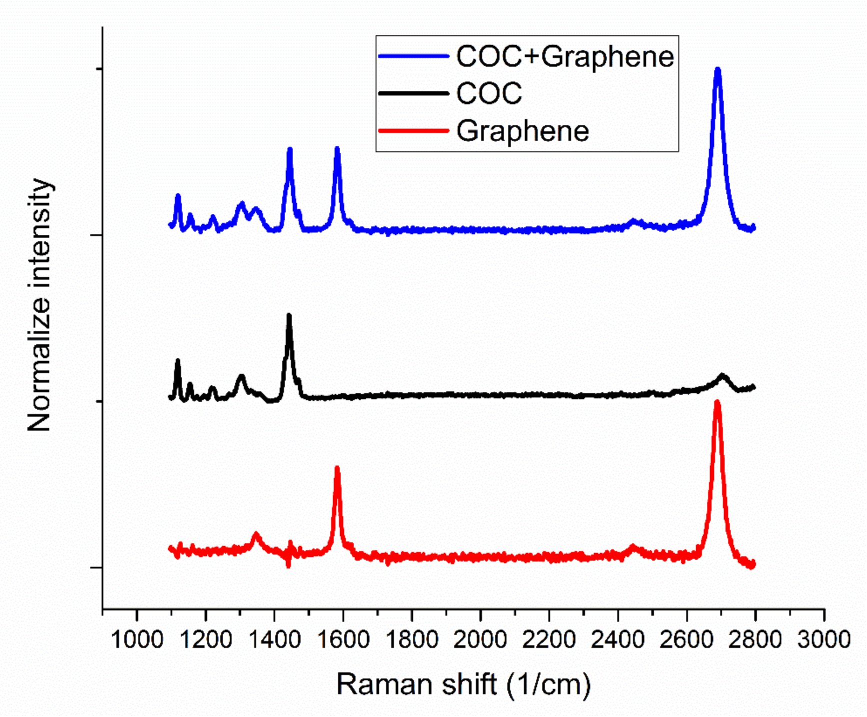

Figure 31 Comparison between the Raman spectra of COC, Graphene and Graphene transferred on COC by hot embossing.

From the Raman spectrum it is clear that the high molding pressure during the hot embossing transfer did not alter the graphene structure and few defects are present.

4.2.2 Photocurrent response

As can be seen in Figure 32, I–V measurements were performed with different incident light intensities ranging from 0 to 15 mW/cm^2. The Gr/Si Schottky junction shows the typical rectifying behavior and works in the backward voltage segment, showing similarities to that of a metal/semiconductor Schottky diode.

From the family of I−V curves, a strong dependence of the device photocurrent on the bias voltage can be seen: for every specific incident light power, the photocurrent increases following the reverse bias rise and saturates when reaches higher reverse biases.

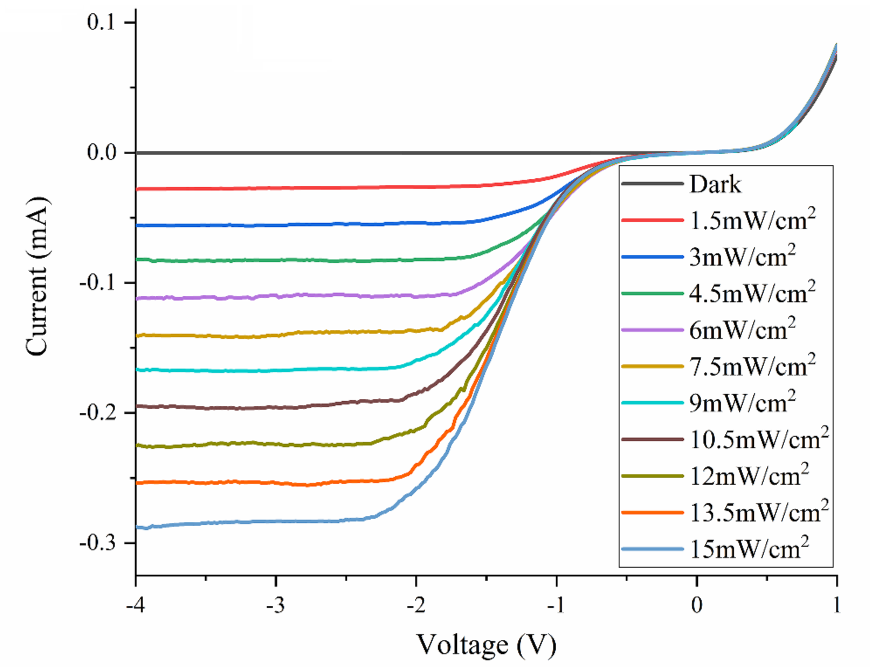

Figure 32 I-V curves for different incident light surface power densities of Gr/n-Si Schottky photodiode.

The energy band diagram shown in Figure 33 explains the photovoltaic characteristic of the Gr/Si Schottky junction which originates this phenomenon.

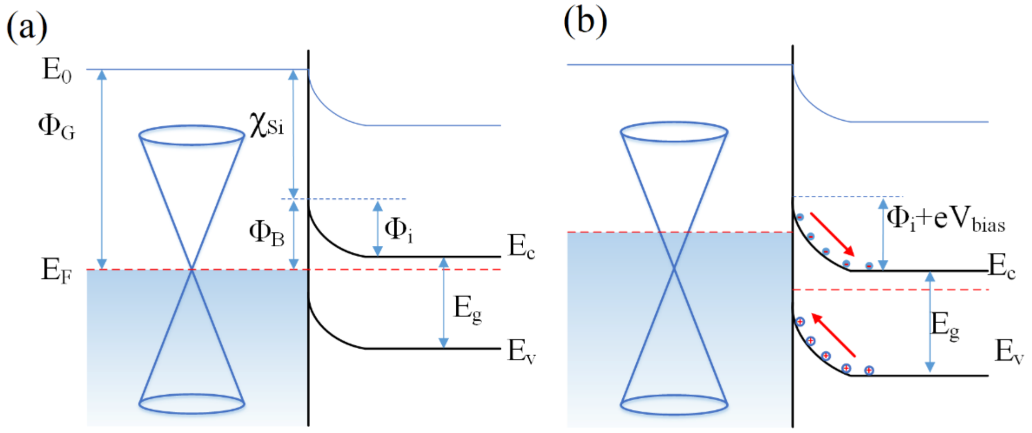

Figure 33 Gr/Si Schottky junction energy band diagram. (a) Energy band diagram at thermal equilibrium of the heterojunction with no incident light. (b) Reverse bias under incident light. E_c, E_v, E_F, E_g, Φ_G, χ_{Si}, Φ_B, and Φ_i denote respectively conduction band, valence band, Fermi level, bandgap, graphene work function, electron affinity of silicon, Schottky barrier height and built-in potential.

The incident photons are absorbed by Si at the graphene/Si interface and excite electron–hole pairs. The built-in potential separates the electron-hole pairs which are transported efficiently to the external electrode thanks to the appropriate biases, where graphene acts as a carrier collector and a high-speed channel for photogenerated carriers.

Figure 33b shows that the built-in potential, Φi, is related to the bias voltage. The bias can tune the ability of charge separation and a relatively large built-in potential helps injecting all of the photoexcited holes from silicon to graphene in order to obtain the saturated photocurrent.

With the application of proper reverse bias on the Gr/Si Schottky junction, the saturated photocurrent increase directly proportional to the incident light surface power density. The time-dependent photoresponse to a pulsed optical signal of various surface power densities with the reverse bias voltage of −3 V is displayed in Figure 34, which demonstrates the reliability and stability of the Gr/Si photodiode fabricated via hot embossing.

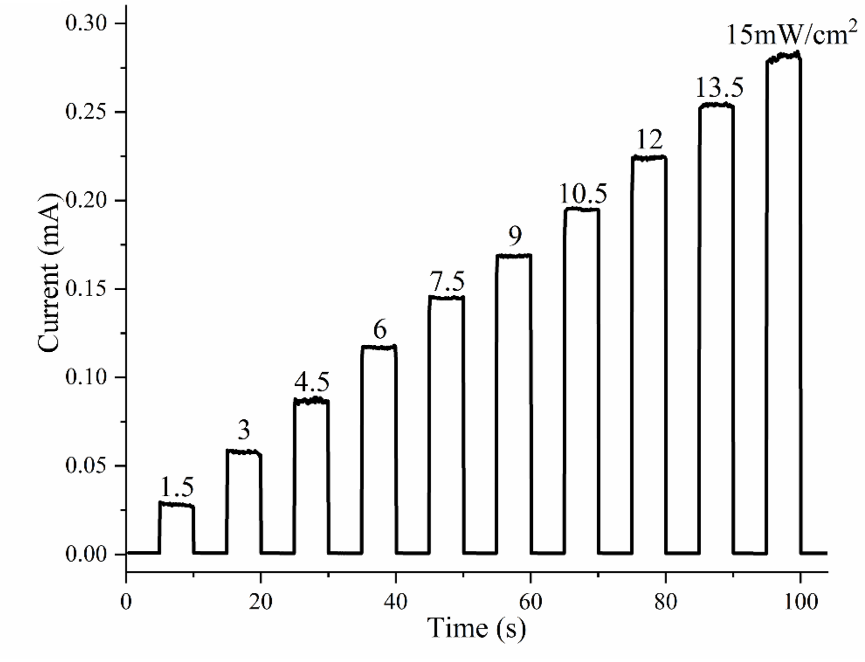

Figure 34 Time dependent photocurrent response.

The hot embossing Gr/n-Si Schottky photodiode showed a measured responsivity of 0.73 A/W. The photoresponses of all the four samples fabricated using the same process were measured when illuminated with different incident light surface power densities and a reverse bias voltage of 3 V. As can be seen in Figure 35, the comparison between the photocurrents shows no substantial differences under the same incident light surface power density, which points out the stability and reliability of the two-step hot embossing process.

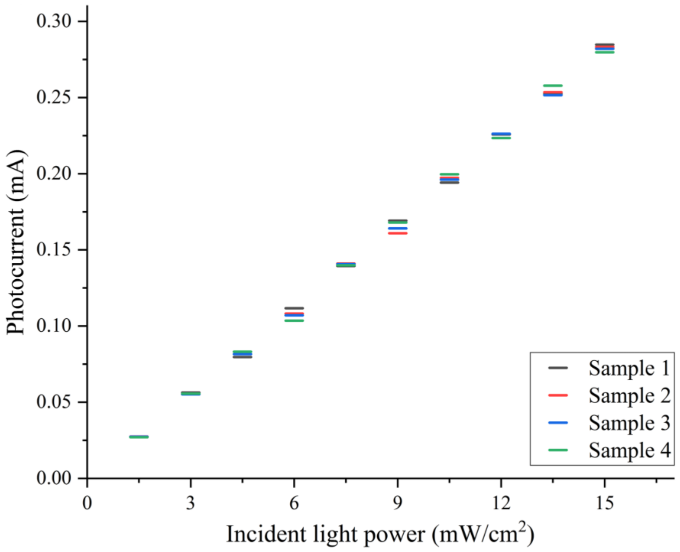

Figure 35 Photocurrent of the four samples under different incident light surface power densities.

4.3.3 Comparison with the models

The hot embossed Gr/Si Schottky photodiode was further investigated by extracting the key Schottky parameters from current–voltage measurements. The current–voltage relation for the Gr/n-Si Schottky junction can be found in the thermionic emission theory,

$$I = I_0(e^{\frac{\mathrm{qV}}{\eta \mathrm{kT}}} - 1) \tag{2}$$

where η is the ideality factor, I_0 is the saturation current defined by

$$I_0 = AA^{*}T^{2}e^{-\frac{\Phi_B}{kT}} \tag{3}$$

where A, A^*, and Φ_B are the diode area, Richardson constant and zero-bias barrier height respectively. When the series resistance (Rs) effect is considered, V in Eq. (2) can be replaced by the difference of the total voltage drop of the system and the voltage drop of series resistance, resulting in two new equations,

$$\frac{\partial V}{\partial(lnI)} = \frac{\eta \mathrm{kT}}{q} + R_S I \tag{4}$$

$$H(I) = R_S I + \eta \Phi_B \tag{5}$$

where H(I) is given by

$$H(I) = V - \eta\left(\frac{kT}{q}\right) ln\left(\frac{I}{AA^{*}T^{2}}\right) \tag{6}$$

According to this, the experimental values of ideality factor η, series resistance R_S, and Schottky barrier height Φ_B can be calculated by Cheung's functions from the non-linear region of the forward bias I–V characteristics.[145,146]

In Figure 36 for the Gr/Si Schottky diode plots of dV/d(lnI) vs I and H(I) vs I are presented. The values of series resistance and ideality factor were calculated from the plot of dV/d(lnI)−I (Figure 36a) and resulted to be respectively 2132 Ω and 2.66 from the intercept and slope of the forward bias, respectively.

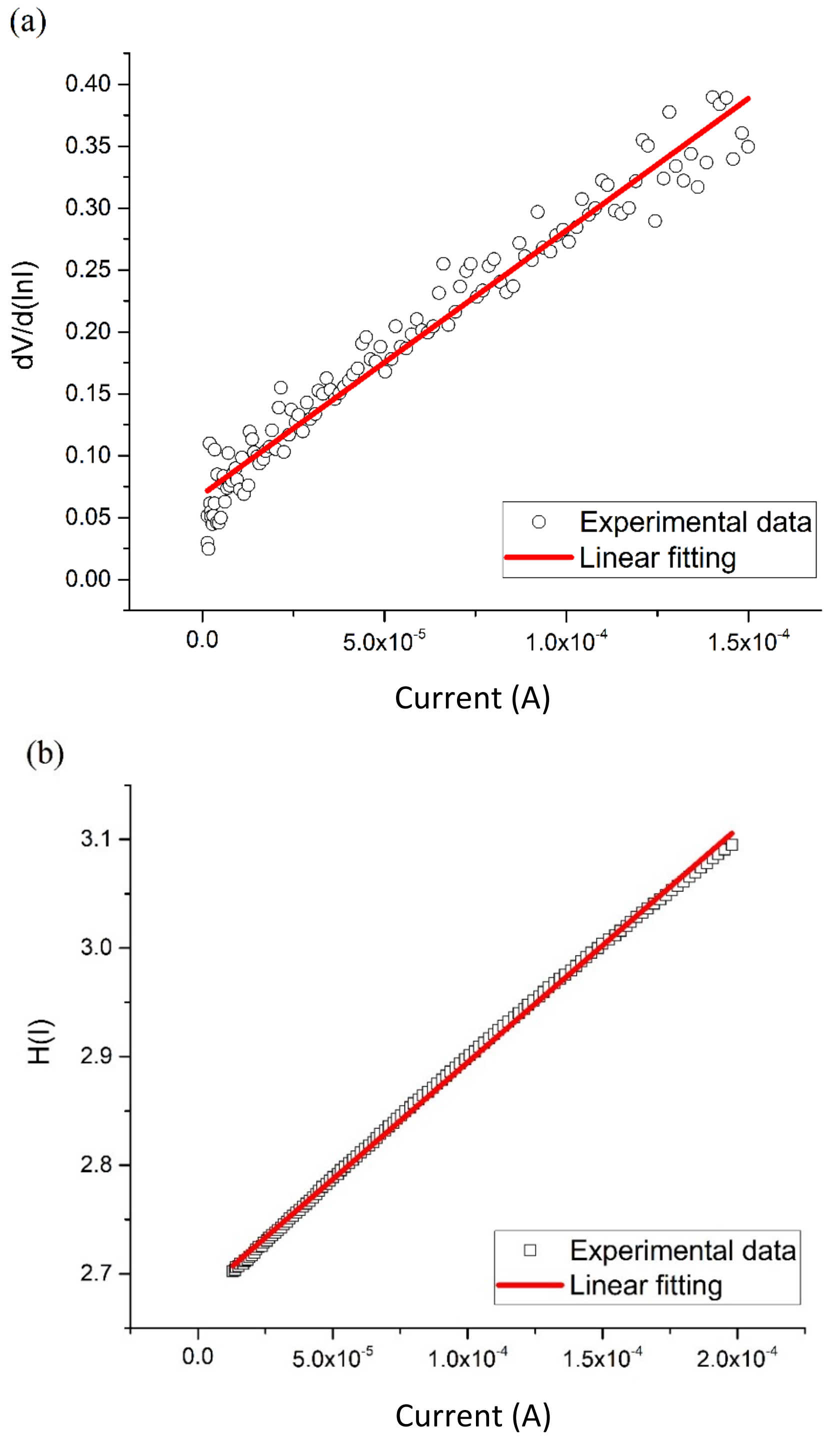

Figure 36 Gr/Si Schottky diode plots of (a) dV/d(ln I) vs I and (b) H(I) vs I.

The Schottky barrier height is found from Eq. (5) from the H(I)−I plot (Figure 36b) thanks to the ideality factor value extracted from the dV/d(lnI)–I plot. Φ_B and Rs are found to be 1.01 eV and 2153 Ω, respectively. The Rs values obtained are very similar, which is a result of the consistency of Cheung's functions.[146]

4.3.4 Comparison with previous literature

Table 2 lists the performances of photodetectors based on graphene: most of them are graphene/Si Schottky structures, while some graphene heterojunction with other materials and some surface modified graphene devices are also included.

Device structure	Responsivity	Schottky barrier height	Series resistance	Ideality factor	Reference
Graphene/Si	0.73 A/W	1.01 eV	2 kΩ	2.66	This work
Graphene/Si	0.73 A/W	—	—	—	147
Graphene/Si	230 mA/W	0.66 eV	6.7 kΩ	1.52	146
Graphene/Si	435 mA/W	—	—	—	148
Graphene/Si	140 mA/W	0.79 eV	32.1 Ω	2.24	149
Graphene/Si	214 mA/W	0.79 eV	—	2.1	150
Graphene/Si	151.9 mA/W	—	—	—	151
Graphene/Si	142 mA/W	0.79 eV	14.9 Ω	—	152
Graphene/Si	0.24 A/W	—	—	—	153
Gr/Si-tips junction	2.5 A/W	0.36 eV	4.5 kΩ	—	154
PEDOT-Graphene/Si	172 mA/W	—	—	—	151
P3HT–Graphene/Si	0.78 A/W	—	—	—	153
TFSA-Graphene/Si	252 mA/W	0.89 eV	10.3 Ω	—	152
MoO3-Graphene/Si	400 mA/W	0.86 eV	17.1 Ω	1.3	149
Graphene/GO/Si	266 mA/W	0.81 eV	—	2.6	150
Graphene/metal	225 mA/W	—	—	—	155
Graphene/Ge	51.8 mA/W	—	—	—	156

Table 2 Summary of photodetectors based on graphene and their performances reported in literature.

The hot embossing fabricated Gr/Si Schottky diode shows a photodetecting ability on the same level of the ones in the literature.

Since in a Schottky photodiode the photogenerated electron–hole pairs are separated by a built-in electric field associated with the Schottky barrier,[157–159] the responsivity of 0.73 A/W is related to the high Schottky barrier height of 1.01 eV. The difference in Schottky barrier height from the other works can be explained with the fact that it is usually calculated with the thermal emission theory, while here was calculated through the Cheung's function. The different methods exploit different data segments for the calculation, resulting in different values.

Neverthless, the series resistance resulted to be more than 2 kΩ, which is higher than the Gr/Si photodiode fabricated by the traditional PMMA-assisted graphene transfer.[147,149]

The high series resistance can be related to the graphene fractures near the silicon window edge, where there is a 300 nm thick SiO_2 step. The high ideality factor can indicate that the complex interface has a negative effect on the device performances.

Despite this, the sensitive, fast, and stable photoresponse demonstrate the feasibility and effectiveness of the reported hot embossing transfer process, which provides a new tool in the graphene devices fabrication.

4.3 Graphene Functionalization

In this section the results on the graphene functionalization are presented. The analysis will cover the data that induced to choose the Caffeic acid for the protocol definition, the comparison between the different incubation steps that resulted in the final protocol and the final study on the different molecules.

4.3.1 Molecule choice

The first screening was made in order to get a basic understanding on the Raman response of the molecules (Raman intensity, peak positions, strong fluorescence background) and to get a set of reference spectra to be compared to the ones after the functionalization: after the incubation in fact the samples were dried and the acquired spectra could be similar to those of the dry molecules, to the solution used for the incubation, a combination of both of them or even slightly different due to the interaction with the graphene surface.

For the second screening, the solubility, the solvents and the position of the peaks were considered. Since the idea was to start with different concentrations to see which one could be the best for the incubation, Triptophane, Pyrene and Protoporphyrin were discarded because they were not soluble enough. Moreover, in the case of Triptophane and Pyrene the intensities of the peaks were quite low, which could influence their detection after the incubation.

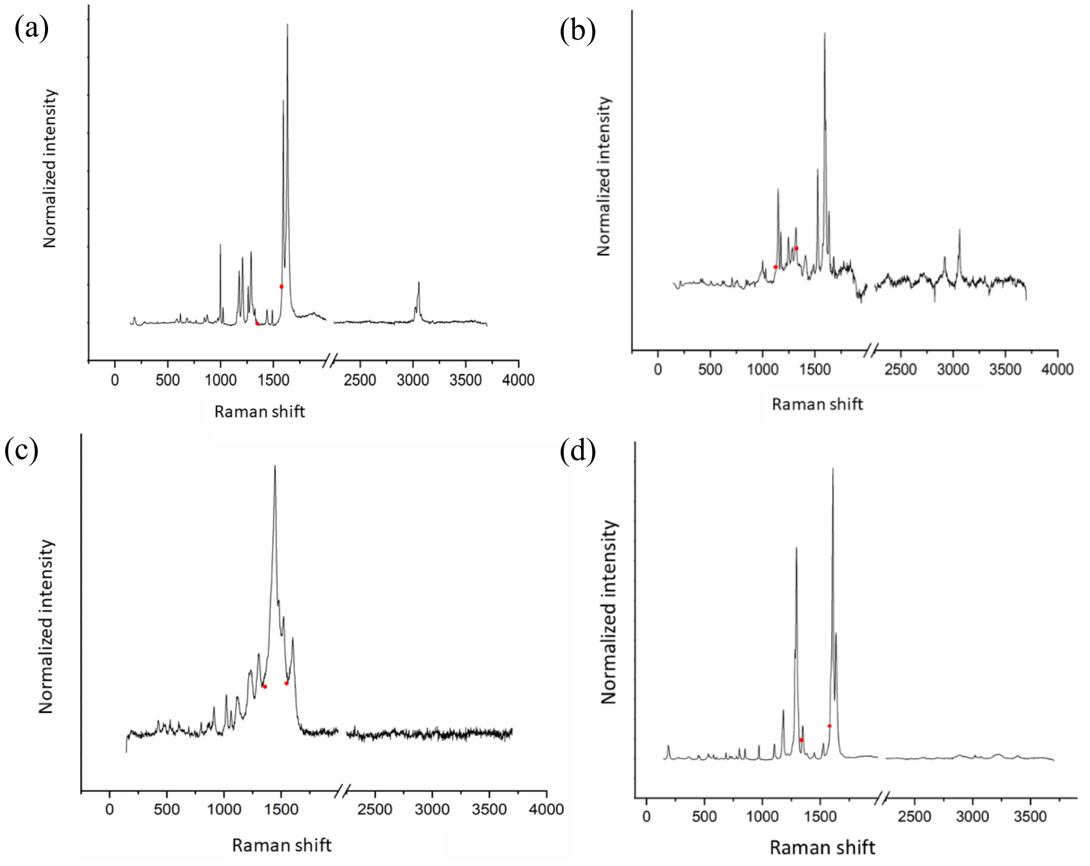

Figure 37 Raman spectra of (a) Trans-cinnamic acid, (b) Benzophenone COOH, (c) Tionine acetate and (d) Caffeic acid in dry state. The usual position of the graphene peaks G and 2D are indicated by the red dots.

Regarding Indole-3-butyric acid, the Raman spectrum had a signal-to-noise ratio worse than the others, so it was discarded as well. Caffeic acid was chosen over Trans-cinnamic acid (Figure 37a) and Benzophenone COOH (Figure 37b) because the graphene main peaks would have been very near to the ones specific to the molecule, which may have created some problems with the analysis. Tionine acetate (Figure 37c) was left apart at first because the functional groups it exposes were less useful for the next required bond with the capture probe.

For the above reasons, the choice ended on Caffeic acid (Figure 37d).

4.3.2 Protocol definition

As described in “3.2.2.4 Protocol definition” the first parameters to choose were the incubation time and the solution concentration. All the possible combinations of the chosen concentrations and times were tried, so the three concentrations were tested for the incubation both overnight and for 1 h.

The average Raman spectra acquired after the incubation evidence that the highest concentration (100 mM) results to be too high for both the incubation times: the Caffeic acid remains onto the samples as a thick coating as demonstrated by the spectra that showed only the main Raman bands of such molecule, without any evidence of graphene (Figure 38). Moreover, also if in the following passages (rinsings) the graphene peaks can be clearly seen, for the data analysis the peaks need to be clearly visible after every step of the process.

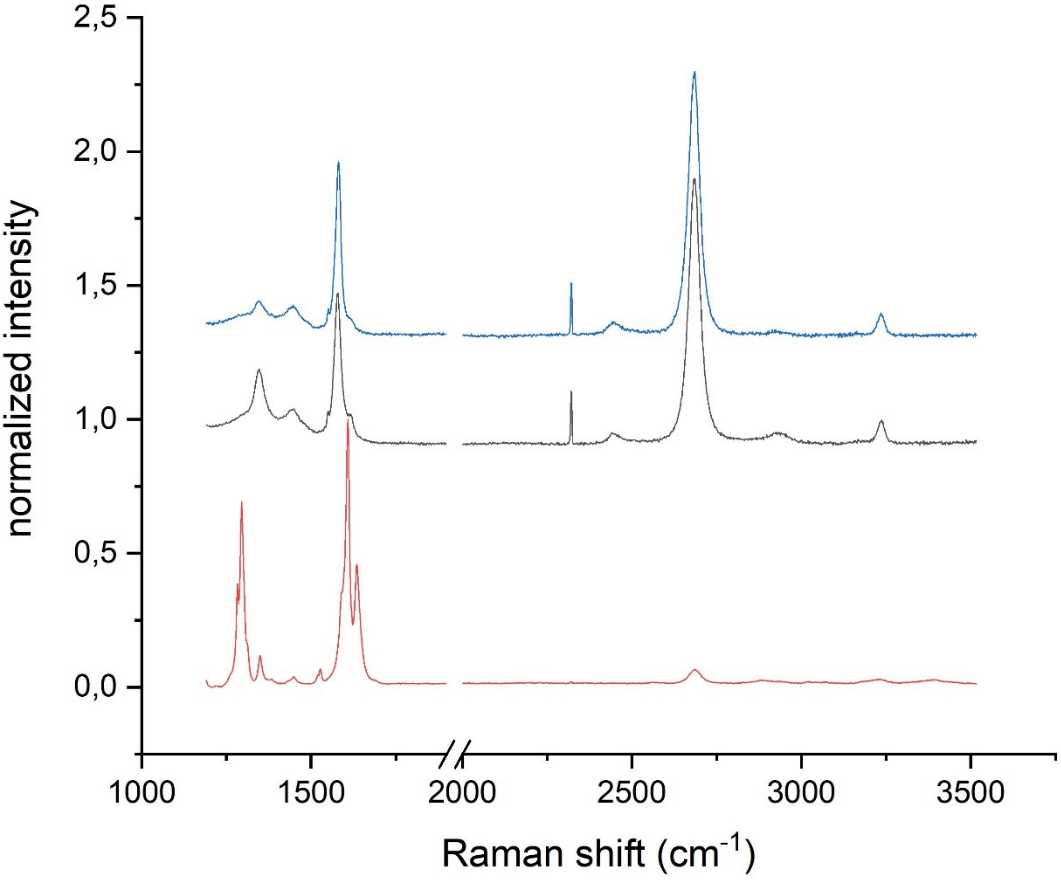

Figure 38 Raman spectra of the sample incubated for 1 h with 100 mM Caffeic acid solution. In red the spectrum after the incubation, in black the graphene spectrum before the incubation and in blue the spectrum after the ethanol rinsing.

For the lowest concentration (1 mM) the quantity of Caffeic acid was too low to be sure that some of it remained onto the graphene, since from the spectra only the graphene peaks could be seen (Figure 39).

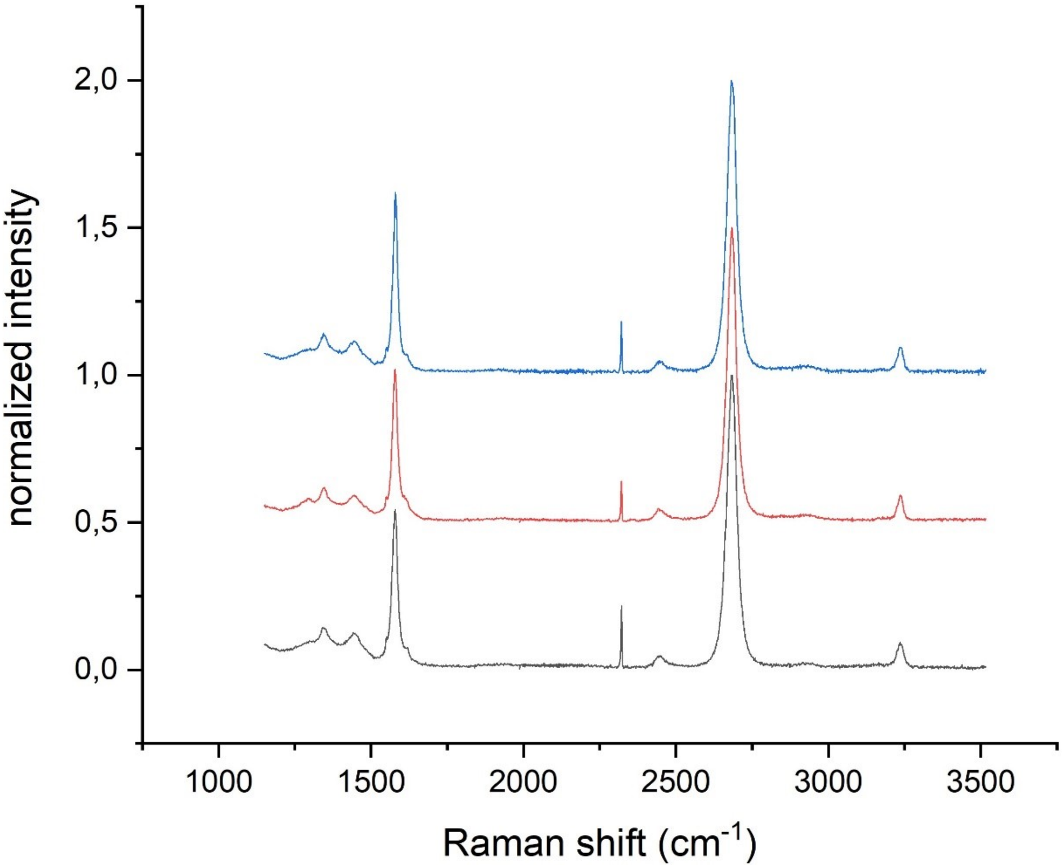

Figure 39 Raman spectra of the sample incubated overnight with 1 mM Caffeic acid solution. In red the spectrum after the incubation, in black the graphene spectrum before the incubation and in blue the spectrum after the ethanol rinsing.

The middle concentration (10 mM) was then chosen, because the caffeic acid spectrum was clearly visible but not so strong to cover the graphene one, ensuring the presence of the molecule and the possibility to compare the graphene peaks with the other passages (Figure 40).

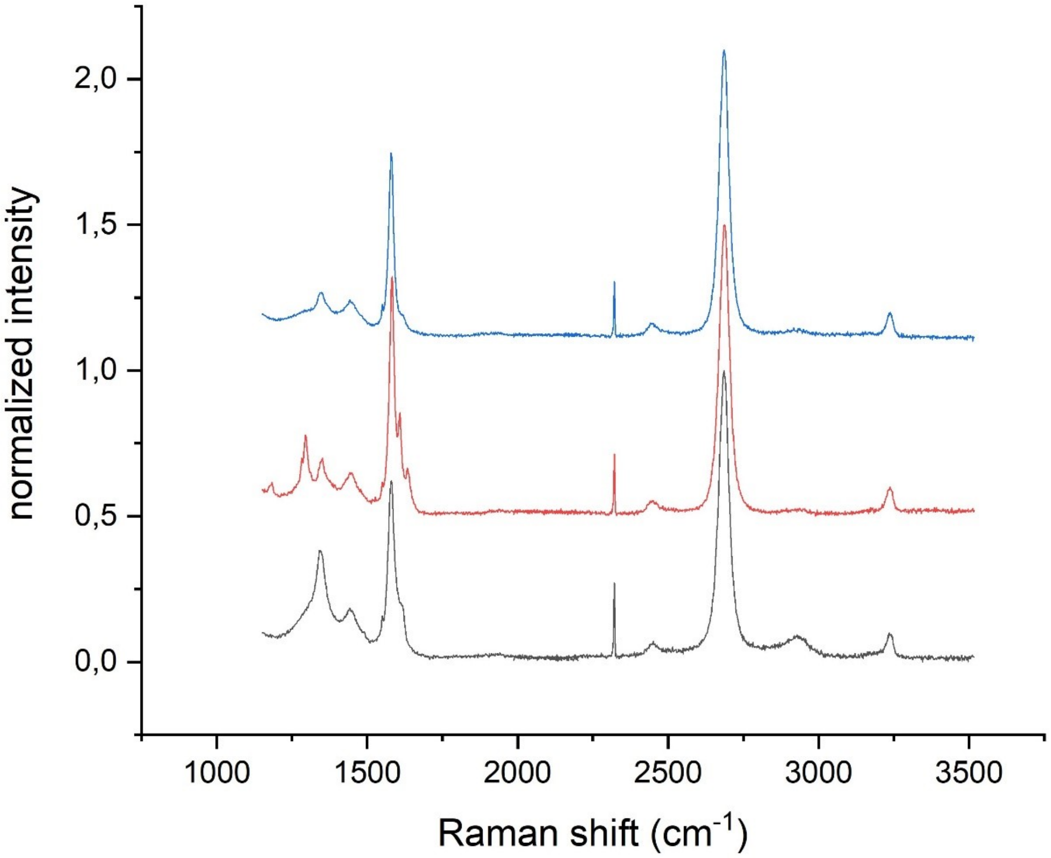

Figure 40 Raman spectra of the sample incubated for 1 h with 10 mM Caffeic acid solution. In red the spectrum after the incubation, in black the graphene spectrum before the incubation and in blue the spectrum after the ethanol rinsing.

Regarding the incubation time, from the reported graphs there seemed to be no significant differences between the two for all the concentrations: for the higher and the lower ones the spectra were identical, while for the middle one the Caffeic acid spectrum was obviously a little weaker, but still clearly visible.

For this reason, 1 hour was chosen, since due to the lack of differences the shorter time had a big advantage in terms of organization and simplification of the work.

Another important time saver arose from this first analysis: the main peaks for both the graphene and Caffeic acid were in the range between 1200 and 2800 cm^{-1}, so the initial two windows for the spectra could be reduced to one, almost halving the time for the spectra acquisition.

4.3.3 Spectra analysis and step comparison

From the spectra of the samples analyzed for the protocol definition, no clear pattern in the peak parameters considered (Intensity, Position, Width and I_D/I_G, I_{2D}/I_G) could be found. However the protocol was different for each sample so new tests were required.

The next test considered 3 samples that had the 2 rinsing steps (Ethanol and PBS, Table 3, Samples 1-3) and 3 samples that missed the ethanol step (Table 3, Samples 4-6). A control sample which was incubated in ethanol only was also considered (Table 3, Control sample).

From the corresponding spectra a clear pattern seemed to rise for the G peak position, as can be retrieved from Table 3.

	Graphene only	After incubation	Rinse with Ethanol	Rinse with PBS	Shift after incubation
Sample 1	1579.1	1580.6	1579.4	1579.2	+ 1.5
Sample 2	1579.3	1583.8	1580.2	1582.9	+ 4.5
Sample 3	1578.9	1584.1	1579.4	1580.6	+ 5.2
Sample 4	1581.3	1583.2		1582.8	+ 1.9
Sample 5	1579.5	1584.0		1580.0	+ 4.5
Sample 6	1580.2	1584.2		1580.0	+ 4.0
Control sample	1580.2	1579.6			- 0.6

Table 3 Graphene G peak position (cm^{-1}) from the Raman spectra taken after every step of the protocol. Samples 1-3 were rinsed first in ethanol and then in PBS after the incubation, while samples 4-6 were rinsed directly in PBS after the incubation. Control sample was incubated in ethanol.

A clear blue-shift is present after the incubation, which is reduced after the rinsing steps but does not disappear, resulting in a small shift in the whole process increasing the G peak position in the samples incubated with Caffeic acid only. The spectra of the control samples did not show remarkable shift at the different steps.

For the other parameters, no clear pattern seems to be present: the values increase and decrease differently from sample to sample without any correlation with the protocol steps.

4.3.4 Other molecules screening

Before going on with the tests of the other molecules, the substrate was changed from Silicon to Gold to avoid the interference of the Silicon spectrum. This was confirmed in a first comparative test following the same protocol and with Gold as a substrate, which resulted in a cleaner and stronger Raman spectrum.

The other remaining molecules were then tested following the same protocol. Regarding Tionine acetate and Protoporphyrin the solubility resulted to be too low and it was clear from the beginning since the molecules did not dissolve completely at the chosen concentration. This resulted in agglomerates that deposited onto the samples and were not removed even after the rinsing steps. For this reason, the analysis could not be performed since the initial spectrum of the molecules remained in all the respective steps and covered the graphene peaks, making impossible to perform any comparison.

In the other cases, only the Benzophenone COOH seemed to exhibit a behavior similar to the one of Caffeic acid, with the G peak that undergoes a shift in position (Table 4).

	Graphene only	After incubation	Rinse with Ethanol	Rinse with DI water	Rinse with PBS	Shift after incubation
Pirene sample	1580.3	1579.8	1579.6		1579.3	- 0.5
Indole-3-butyric acid sample	1579.6	1579.7	1578.2		1578.0	+ 0.1
Trans-cinnamic acid sample	1580.0	1579.7	1579.2		1579.1	- 0.3
Benzophenone COOH sample	1579.0	1582.9	1581.5		1580.3	+ 3.9
Triptophane sample	1578.7	1578.2		1578.6	1578.5	- 0.5

Table 4 Graphene G peak position (cm^{-1}) from the Raman spectra taken after every step of the protocol for the different molecules.

The analysis of course is not definitive, since only one sample was tested for every molecule. A few repetitions are required to assess if the response from these molecules is really negative.

5 Chapter

Conclusions and future outlooks

In this final chapter the main results of this work and the future planned or suggested improvements are discussed.

Starting from the literature knowledge, a working graphene Field Effect Transistor on Silicon has been fabricated. The transistor was tested in the electrolyte-gated setup showing the expected electrical characteristics, while graphene demonstrated to maintain the monolayer behavior.

The next step was the improvement of the graphene transfer process: other than avoiding some problems from the standard PMMA-assisted transfer like PMMA induced impurities, the idea was to replace an extremely operator-dependent step by a more standardized process. graphene was therefore successfully transferred via Hot Embossing on a 140 μm thick COC substrate.

The process demonstrated that standard lithography can be performed on that substrate and a completely functional G-FET can be fabricated on a polymer substrate. Graphene transferred this way showed characteristics comparable with the previous transfer, and the Raman analysis showed no substantial differences between the two.

G-FETs fabricated this way were tested as strain and pH sensors, showing promising behavior for other application in the sensor field. Being the COC a flexible substrate, the G-FET grants the possibility for this transfer process to be exploited in the flexible electronics field.

In the near future G-FETs are planned to be tested for live sensing of biomarkers and antibiotics: a microfluidic platform has been fabricated by a fellow PhD student and some protocols for the functionalization of the Au gate have been defined. A solution of the selected analyte will be fluxed in the sealed chamber that forms the G-FET, where previously determined V_g and V_{ds} are imposed. The tests should show a change in I_{ds} during the solution flow due to the binding of the analyte to the functionalized gate, demonstrating the detection of the molecule.

Exploiting the same Hot Embossing transfer process, a Schottky diode has been fabricated. The process showed the possibility to implement the transfer in other devices fabrication and successfully demonstrated the advantages of a transparent substrate that allows light passing and can be useful as a packaging layer, protecting the device.

The Schottky diode was compared with the literature and showed promising behavior, a good photocurrent response and characteristics comparable to other devices.

The possibility of a second Embossing transfer was demonstrated, and the Raman spectrum showed that graphene is not influenced in his behavior by it, providing an even easier transfer process when graphene does not need to be exposed to the environment but can be covered by the polymeric substrate.

The feasibility of this transfer technique in the optics field with its advantages is clear. In the future the device could be implemented in a more complex system, while the transfer process could be tested for the fabrication of other optical devices where graphene could improve the device behavior.

In parallel with the previous works, a protocol for graphene functionalization has been defined. After a first selection of molecules, caffeic acid has been chosen and studied thoroughly to find the best protocol for the functionalization. The Raman spectra showed a shift in the G peak position of graphene, which can be correlated to the formation of a monolayer of caffeic acid on the graphene structure bonded together.

Other molecules have been tested with the same protocol for a broad range of possible graphene functionalizations, but the results are still preliminary and will need further tests for a clear view of the bonding possibilities.

Further tests are planned for the confirmation of the creation of the functionalized monolayer on graphene: colorimetric measures will be performed to demonstrate the bonding between graphene and the molecules under study.

The next step requires that after the confirmation of the π-π stacking of the molecule onto graphene, the final capture probe for the detection will be attached to the bridge molecule.

After the definition of all the functionalization steps, the functionalization will be implemented in the sensor device and the work will focus on optimizing the fabrication process in order to obtain the lowest LOD (Limit of Detection) for the detection of both lung cancer biomarkers and antibiotics in food. A finalized device could be also exploited for other different analytes detection, with a small change in the functionalization probe and/or bridge molecule.

In conclusion, Graphene has shown to be a promising material, exploitable for the fabrication of G-FETs and G-FETs biosensors on polymer materials. The transfer process on polymeric substrates allows to avoid the many problems that arise with the standard PMMA assisted transfer, and the Graphene itself shows promising results for its functionalization toward a sensoristic purpose.

References

1. Wang, X., Cheng, Z., Xu, K., Tsang, H. K. & Xu, J.-B. High-responsivity graphene/silicon-heterostructure waveguide photodetectors. *Nat. Photonics* **7**, 888–891 (2013).
2. Geng, D., Wang, H. & Yu, G. Graphene single crystals: Size and morphology engineering. *Advanced Materials* **27**, 2821–2837 (2015).
3. McNerny, D. Q. *et al.* Direct fabrication of graphene on SiO2 enabled by thin film stress engineering. *Sci. Rep.* **4**, 5049 (2015).
4. Mohsin, A. *et al.* Synthesis of millimeter-size hexagon-shaped graphene single crystals on resolidified copper. *ACS Nano* **7**, 8924–8931 (2013).
5. Han, F. *et al.* A highly efficient synthetic process of graphene films with tunable optical properties. *Appl. Surf. Sci.* **314**, 71–77 (2014).
6. Papageorgiou, D. G., Kinloch, I. A. & Young, R. J. Mechanical properties of graphene and graphene-based nanocomposites. *Progress in Materials Science* **90**, 75–127 (2017).
7. Papageorgiou, D. G., Kinloch, I. A. & Young, R. J. Mechanical properties of graphene and graphene-based nanocomposites. *Progress in Materials Science* **90**, 75–127 (2017).
8. Geim, A. K. Nobel Lecture: Random walk to graphene *. *APS* **83**, 851–862 (2011).
9. Yi, M. & Shen, Z. A review on mechanical exfoliation for the scalable production of graphene. *Journal of Materials Chemistry A* **3**, 11700–11715 (2015).
10. Shmavonyan, G., Aroutiounian, V. M., Sh SHMAVONYAN, G. & Sevoyan, G. *Enlarging the surface area of monolayer graphene synthesized by mechanical exfoliation*. *Armenian Journal of Physics* **6**, (2013).
11. Xu, W., Mao, N. & Zhang, J. Graphene: A platform for surface-enhanced Raman spectroscopy. *Small* **9**, 1206–1224 (2013).
12. Moon, I. K., Lee, J., Ruoff, R. S. & Lee, H. Reduced graphene oxide by chemical graphitization. *Nat. Commun.* **1**, 1–6 (2010).
13. Pei, S. & Cheng, H. M. The reduction of graphene oxide. *Carbon N. Y.* **50**, 3210–3228 (2012).
14. Shao, G. *et al.* Graphene oxide: The mechanisms of oxidation and exfoliation. *Journal of Materials Science* **47**, 4400–4409 (2012).
15. Stankovich, S. *et al.* Synthesis of graphene-based nanosheets via chemical reduction of exfoliated graphite oxide. *Carbon N. Y.* **45**, 1558–1565 (2007).
16. Guoxiu, W. *et al.* Facile synthesis and characterization of graphene nanosheets. *J. Phys. Chem. C* **112**, 8192–8195 (2008).
17. Chen, W., Yan, L. & Bangal, P. R. Chemical reduction of graphene oxide to graphene by sulfur-containing compounds. *J. Phys. Chem. C* **114**, 19885–19890 (2010).
18. Chua, C., Reviews, M. P.-C. S. & 2014, undefined. Chemical reduction of graphene oxide: a synthetic chemistry viewpoint. *pubs.rsc.org*
19. Tadyszak, K., Wychowaniec, J. & Litowczenko, J. Biomedical Applications of Graphene-Based Structures. *Nanomaterials* **8**, 944 (2018).
20. Hernandez, Y. *et al.* High-yield production of graphene by liquid-phase exfoliation of graphite. *Nat. Nanotechnol.* **3**, 563–568 (2008).
21. Niu, L. *et al.* Production of Two-Dimensional Nanomaterials via Liquid-Based Direct Exfoliation. *Small* **12**, 272–293 (2016).

22. Ciesielski, A., Samorı`*, P. & Samorı`*, S. Graphene via sonication assisted liquid-phase exfoliation †. *Chem. Soc. Rev* **43**, 381 (2014).
23. Paton, K. *et al.* Scalable production of large quantities of defect-free few-layer graphene by shear exfoliation in liquids. *nature.com*
24. Dimiev, A. M., Ceriotti, G., Metzger, A., Kim, N. D. & Tour, J. M. Chemical mass production of graphene nanoplatelets in ∼100% yield. *ACS Nano* **10**, 274–279 (2016).
25. Cui, X., Zhang, C., Hao, R. & Hou, Y. Liquid-phase exfoliation, functionalization and applications of graphene. *Nanoscale* **3**, 2118–2126 (2011).
26. Emtsev, K. V. *et al.* Towards wafer-size graphene layers by atmospheric pressure graphitization of silicon carbide. *Nat. Mater.* **8**, 203–207 (2009).
27. Li, X. *et al.* Large-area synthesis of high-quality and uniform graphene films on copper foils. *Science (80-.).* **324**, 1312–1314 (2009).
28. Srivastava, A. *et al.* Novel liquid precursor-based facile synthesis of large-area continuous, single, and few-layer graphene films. *Chem. Mater.* **22**, 3457–3461 (2010).
29. Dong, X. *et al.* Growth of large-sized graphene thin-films by liquid precursor-based chemical vapor deposition under atmospheric pressure. *Elsevier*
30. Ruan, G., Sun, Z., Peng, Z. & Tour, J. M. Growth of graphene from food, insects, and waste. *ACS Nano* **5**, 7601–7607 (2011).
31. Ago, H. CVD growth of high-quality single-layer graphene. in *Frontiers of Graphene and Carbon Nanotubes: Devices and Applications* 3–20 (Springer Japan, 2015). doi:10.1007/978-4-431-55372-4_1
32. Novoselov, K. S., Mishchenko, A., Carvalho, A. & Castro Neto, A. H. 2D materials and van der Waals heterostructures. *Science* **353**, (2016).
33. Tour, J. M. Top-down versus bottom-up fabrication of graphene-based electronics. *Chemistry of Materials* **26**, 163–171 (2014).
34. Cai, J. *et al.* Atomically precise bottom-up fabrication of graphene nanoribbons. *Nature* **466**, 470–473 (2010).
35. Narita, A. *et al.* Synthesis of structurally well-defined and liquid-phase-processable graphene nanoribbons. *Nat. Chem.* **6**, 126–132 (2014).
36. Dössel, L., Gherghel, L., Feng, X. & Müllen, K. Graphene nanoribbons by chemists: Nanometer-sized, soluble, and defect-free. *Angew. Chemie - Int. Ed.* **50**, 2540–2543 (2011).
37. Zhi, L. & Müllen, K. A bottom-up approach from molecular nanographenes to unconventional carbon materials. *J. Mater. Chem.* **18**, 1472–1484 (2008).
38. Narita, A. *et al.* Bottom-up synthesis of liquid-phase-processable graphene nanoribbons with near-infrared absorption. *ACS Nano* **8**, 11622–11630 (2014).
39. Talirz, L. *et al.* Termini of bottom-up fabricated graphene nanoribbons. *J. Am. Chem. Soc.* **135**, 2060–2063 (2013).
40. Narita, A., Feng, X. & Müllen, K. Bottom-up synthesis of chemically precise graphene nanoribbons. *Chem. Rec.* **15**, 295–309 (2015).
41. Raccichini, R., Varzi, A., Passerini, S. & Scrosati, B. The role of graphene for electrochemical energy storage. *Nat. Mater.* **14**, 271–279 (2015).
42. Cooper, A. J. *et al.* How to Get Between the Sheets: A Review of Recent Works on the Electrochemical Exfoliation of Graphene Materials from Bulk Graphite. *pubs.rsc.org* **7**, 6944 (2015).
43. Yu, P., Lowe, S. E., Simon, G. P. & Zhong, Y. L. Electrochemical exfoliation

of graphite and production of functional graphene. *Current Opinion in Colloid and Interface Science* **20**, 329–338 (2015).

44. Low, C., Walsh, F., Chakrabarti, M., Carbon, M. H.- & 2013, undefined. Electrochemical approaches to the production of graphene flakes and their potential applications. *Elsevier*
45. Sood, A. K. *et al.* Review of Graphene Technology and Its Applications for Electronic Devices. in *Graphene - New Trends and Developments* (InTech, 2015). doi:10.5772/61316
46. Gupta, G., Zeng, M., Nurbawono, A., Huang, W. & Liang, G. Applications of graphene-based materials in electronic devices. in *Graphene Science Handbook: Applications and Industrialization* 279–297 (CRC Press, 2016). doi:10.1201/b19488-23
47. Nag, A., Mitra, A. & Mukhopadhyay, S. C. Graphene and its sensor-based applications: A review. *Sensors and Actuators, A: Physical* **270**, 177–194 (2018).
48. Sojoudi, H., Baltazar, J., Tolbert, L. M., Henderson, C. L. & Graham, S. Creating graphene p-n junctions using self-assembled monolayers. *ACS Appl. Mater. Interfaces* **4**, 4781–4786 (2012).
49. Schwierz, F. Graphene transistors. *Nature Nanotechnology* **5**, 487–496 (2010).
50. Szafranek, B. N., Fiori, G., Schall, D., Neumaier, D. & Kurz, H. Current saturation and voltage gain in bilayer graphene field effect transistors. *Nano Lett.* **12**, 1324–1328 (2012).
51. Avouris, P. & Dimitrakopoulos, C. Graphene: Synthesis and applications. *Materials Today* **15**, 86–97 (2012).
52. Gao, Y. *et al.* High-speed electro-optic modulator integrated with graphene-boron nitride heterostructure and photonic crystal nanocavity. *Nano Lett.* **15**, 2001–2005 (2015).
53. Gan, X. *et al.* Controlled light-matter interaction in graphene electrooptic devices using nanophotonic cavities and waveguides. *IEEE J. Sel. Top. Quantum Electron.* **20**, (2014).
54. Ooi, K. J. A., Chu, H. S., Bai, P. & Ang, L. K. Electro-optical graphene plasmonic logic gates. *Opt. Lett.* **39**, 1629 (2014).
55. Strikha, M. V. & Vasko, F. T. Electro-optics of graphene: Field-modulated reflection and birefringence. *Phys. Rev. B - Condens. Matter Mater. Phys.* **81**, 115413 (2010).
56. Ooi, K. J. A., Ang, L. K. & Tan, D. T. H. Waveguide engineering of graphene’s nonlinearity. *Appl. Phys. Lett.* **105**, 111110 (2014).
57. Lee, C.-C., Suzuki, S., Xie, W. & Schibli, T. R. Broadband graphene electro-optic modulators with sub-wavelength thickness. *Opt. Express* **20**, 5264 (2012).
58. Review, M. R.-O.-E. & 1998, undefined. Current status and future trends of infrared detectors. *infona.pl*
59. Cai, X. *et al.* Sensitive room-temperature terahertz detection via the photothermoelectric effect in graphene. *nature.com* (2014). doi:10.1038/NNANO.2014.182
60. Yan, J. *et al.* Dual-gated bilayer graphene hot-electron bolometer. *Nat. Nanotechnol.* **7**, 472–478 (2012).
61. Ryzhii, V., Otsuji, T., Ryzhii, M. & Shur, M. S. Double graphene-layer plasma resonances terahertz detector. *J. Phys. D. Appl. Phys.* **45**, (2012).
62. Freitag, M., Low, T. & Avouris, P. Increased responsivity of suspended

graphene photodetectors. *Nano Lett.* **13**, 1644–1648 (2013).

63. Du, X., Prober, D. E., Vora, H. & Mckitterick, C. B. Graphene-based Bolometers. (2014). doi:10.2478/gpe-2014-0001
64. Klekachev, A. V. *et al.* Graphene transistors and photodetectors. *Electrochem. Soc. Interface* **22**, 63–68 (2013).
65. Tunable Graphene-Based Method for Detecting Mid-Infrared (IR) Radiation - 33901 - University of Central Florida. Available at: https://technologies.tt.research.ucf.edu/technologies/33901_tunable-graphene-based-method-for-detecting-mid-infrared-ir-radiation. (Accessed: 8th January 2021)
66. Pumera, M., Ambrosi, A., Bonanni, A., Chng, E. L. K. & Poh, H. L. Graphene for electrochemical sensing and biosensing. *TrAC - Trends in Analytical Chemistry* **29**, 954–965 (2010).
67. Shan, C. *et al.* Direct electrochemistry of glucose oxidase and biosensing for glucose based on graphene. *Anal. Chem.* **81**, 2378–2382 (2009).
68. Kang, X. *et al.* Glucose oxidase–graphene–chitosan modified electrode for direct electrochemistry and glucose sensing. *Elsevier*
69. Luo, J. *et al.* A novel non-enzymatic glucose sensor based on Cu nanoparticle modified graphene sheets electrode. *Elsevier*
70. Liu, M., Liu, R., Bioelectronics, W. C.-B. and & 2013, undefined. Graphene wrapped Cu2O nanocubes: non-enzymatic electrochemical sensors for the detection of glucose and hydrogen peroxide with enhanced stability. *Elsevier*
71. Zhang, Y., Wang, Y., Jia, J., Chemical, J. W.-S. and A. B. & 2012, undefined. Nonenzymatic glucose sensor based on graphene oxide and electrospun NiO nanofibers. *Elsevier*
72. Dey, R. S. & Raj, C. R. Development of an amperometric cholesterol biosensor based on graphene-Pt nanoparticle hybrid material. *J. Phys. Chem. C* **114**, 21427–21433 (2010).
73. He, Y. *et al.* Magnetite–graphene for the direct electrochemistry of hemoglobin and its biosensing application. *Elsevier*
74. Wu, J., Xu, M., Communications, G. Z.-E. & 2010, undefined. Graphene-based modified electrode for the direct electron transfer of cytochrome c and biosensing. *Elsevier*
75. Sundar Dey, R. & Retna Raj, C. Redox-Functionalized Graphene Oxide Architecture for the Development of Amperometric Biosensing Platform. *ACS Appl. Mater. Interfaces* **5**, 27 (2013).
76. Xu, H. *et al.* Graphene-based nanoprobes and a prototype optical biosensing platform. *Elsevier*
77. Lv, W. *et al.* DNA-dispersed graphene/NiO hybrid materials for highly sensitive non-enzymatic glucose sensor. *Elsevier*
78. Yuan, B. *et al.* Graphene oxide/nickel oxide modified glassy carbon electrode for supercapacitor and nonenzymatic glucose sensor. *Elsevier*
79. Unnikrishnan, B., Palanisamy, S., Bioelectronics, S. C.-B. and & 2013, undefined. A simple electrochemical approach to fabricate a glucose biosensor based on graphene–glucose oxidase biocomposite. *Elsevier*
80. Chen, T., Loan, P., Hsu, C., … Y. L.-B. and & 2013, undefined. Label-free detection of DNA hybridization using transistors based on CVD grown graphene. *Elsevier*
81. Bo, Y. *et al.* A novel electrochemical DNA biosensor based on graphene and polyaniline nanowires. *Elsevier*
82. Hu, Y. *et al.* Label-free electrochemical impedance sensing of DNA

hybridization based on functionalized graphene sheets. *Chem. Commun.* **47**, 1743–1745 (2011).
83. Dong, H., Zhu, Z., Ju, H., Bioelectronics, F. Y.-B. and & 2012, undefined. Triplex signal amplification for electrochemical DNA biosensing by coupling probe-gold nanoparticles–graphene modified electrode with enzyme. *Elsevier*
84. Zhou, M., Zhai, Y. & Dong, S. Electrochemical sensing and biosensing platform based on chemically reduced graphene oxide. *Anal. Chem.* **81**, 5603–5613 (2009).
85. Gao, F. *et al.* Highly sensitive and selective detection of dopamine in the presence of ascorbic acid at graphene oxide modified electrode. *Elsevier*
86. Li, S. *et al.* Electrochemical detection of dopamine using water-soluble sulfonated graphene. *Elsevier*
87. Yang, L., Liu, D., Huang, J., Chemical, T. Y.-S. and A. B. & 2014, undefined. Simultaneous determination of dopamine, ascorbic acid and uric acid at electrochemically reduced graphene oxide modified electrode. *Elsevier*
88. Hernandez, F. J. & Ozalp, V. C. Graphene and other nanomaterial-based electrochemical aptasensors. *Biosensors* **2**, 1–14 (2012).
89. Bae, S. *et al.* Graphene-based transparent strain sensor. *Elsevier*
90. Tian, H. *et al.* Scalable fabrication of high-performance and flexible graphene strain sensors. *Nanoscale* **6**, 699–705 (2014).
91. Qin, Y. *et al.* Lightweight, Superelastic, and Mechanically Flexible Graphene/Polyimide Nanocomposite Foam for Strain Sensor Application. *ACS Nano* **9**, 8933–8941 (2015).
92. Xu, Y. *et al.* In-plane and tunneling pressure sensors based on graphene/hexagonal boron nitride heterostructures. *Appl. Phys. Lett.* **99**, (2011).
93. Trung, T. Q. & Lee, N. E. Flexible and Stretchable Physical Sensor Integrated Platforms for Wearable Human-Activity Monitoringand Personal Healthcare. *Adv. Mater.* **28**, 4338–4372 (2016).
94. Ryu, S. *et al.* Extremely Elastic Wearable Carbon Nanotube Fiber Strain Sensor for Monitoring of Human Motion. *ACS Nano* **9**, 5929–5936 (2015).
95. Viventi, J., Kim, D., Moss, J., … Y. K.-S. translational & 2010, undefined. A conformal, bio-interfaced class of silicon electronics for mapping cardiac electrophysiology. *stm.sciencemag.org*
96. Chang, N. K., Su, C. C. & Chang, S. H. Fabrication of single-walled carbon nanotube flexible strain sensors with high sensitivity. *Appl. Phys. Lett.* **92**, (2008).
97. Lipomi, D., Vosgueritchian, M., … B. T.-N. & 2011, undefined. Skin-like pressure and strain sensors based on transparent elastic films of carbon nanotubes. *nature.com*
98. Zhou, J., Yu, H., Xu, X., Han, F. & Lubineau, G. Ultrasensitive, Stretchable Strain Sensors Based on Fragmented Carbon Nanotube Papers. *ACS Publ.* **9**, 4835–4842 (2017).
99. Wang, Y. *et al.* Ultra-sensitive graphene strain sensor for sound signal acquisition and recognition. *Springer* doi:10.1007/s12274-014-0652-3
100. Li, X. *et al.* Multifunctional graphene woven fabrics. *nature.com*
101. Yan, C. *et al.* Highly stretchable piezoresistive graphene-nanocellulose nanopaper for strain sensors. *Adv. Mater.* **26**, 2022–2027 (2014).
102. Bae, S. H. *et al.* Graphene-based transparent strain sensor. *Carbon N. Y.* **51**,

236–242 (2013).

103. Inaba, A., Yoo, G., Takei, Y., … K. M.-2013 I. 26th & 2013, undefined. A graphene FET gas sensor gated by ionic liquid. *ieeexplore.ieee.org*

104. Kim, C., Yoo, S., Nam, D., … S. S.-I. electron device & 2012, undefined. Effect of Temperature and Humidity on and Gas Sensitivity of Bottom-Gate Graphene FETs Prepared by ICP-CVD. *ieeexplore.ieee.org*

105. Fu, W. *et al. High mobility graphene ion-sensitive field-effect transistors by noncovalent functionalization*. *pubs.rsc.org*

106. Maehashi, K., Sofue, Y., Okamoto, S., … Y. O.-S. and A. B. & 2013, undefined. Selective ion sensors based on ionophore-modified graphene field-effect transistors. *Elsevier*

107. Zhang, T. *et al.* Self-assembled 1-octadecanethiol monolayers on graphene for mercury detection. *Nano Lett.* **10**, 4738–4741 (2010).

108. Sudibya, H. G., He, Q., Zhang, H. & Chen, P. Electrical detection of metal ions using field-effect transistors based on micropatterned reduced graphene oxide films. *ACS Nano* **5**, 1990–1994 (2011).

109. Gautam, M. & Jayatissa, A. H. Graphene based field effect transistor for the detection of ammonia. *J. Appl. Phys.* **112**, (2012).

110. Zhang, Z. *et al.* Hydrogen gas sensor based on metal oxide nanoparticles decorated graphene transistor †. *pubs.rsc.org* **7**, 10078 (2015).

111. Mailly-Giacchetti, B. *et al.* pH sensing properties of graphene solution-gated field-effect transistors. *J. Appl. Phys* **114**, 84505 (2013).

112. Ang, P. K., Chen, W., Wee, A. T. S. & Kian, P. L. Solution-gated epitaxial graphene as pH sensor. *J. Am. Chem. Soc.* **130**, 14392–14393 (2008).

113. Ohno, Y., Maehashi, K., Yamashiro, Y. & Matsumoto, K. Electrolyte-gated graphene field-effect transistors for detecting ph and protein adsorption. *Nano Lett.* **9**, 3318–3322 (2009).

114. Sohn, I. *et al.* pH sensing characteristics and biosensing application of solution-gated reduced graphene oxide field-effect transistors. *Elsevier*

115. Lei, N., Li, P., Xue, W. & Xu, J. Simple graphene chemiresistors as pH sensors: Fabrication and characterization. *Meas. Sci. Technol.* **22**, 107002 (2011).

116. Wen, Y. *et al.* The Electrical Detection of Lead Ions Using Gold-Nanoparticle-and DNAzyme-Functionalized Graphene Device. *spms.ntu.edu.sg* (2012). doi:10.1002/adhm.201200220

117. Liu, Y., Dong, X. & Chen, P. Biological and chemical sensors based on graphene materials. *Chem. Soc. Rev.* **41**, 2283–2307 (2012).

118. Georgakilas, V. *et al.* Functionalization of graphene: Covalent and non-covalent approaches, derivatives and applications. *Chemical Reviews* **112**, 6156–6214 (2012).

119. Georgakilas, V. *et al.* Noncovalent Functionalization of Graphene and Graphene Oxide for Energy Materials, Biosensing, Catalytic, and Biomedical Applications. *Chemical Reviews* **116**, 5464–5519 (2016).

120. Niyogi, S. *et al.* Spectroscopy of covalently functionalized graphene. *Nano Lett.* **10**, 4061–4066 (2010).

121. Kosynkin, D. V. *et al.* Longitudinal unzipping of carbon nanotubes to form graphene nanoribbons. *Nature* **458**, 872–876 (2009).

122. Sinitskii, A. *et al.* Kinetics of diazonium functionalization of chemically converted graphene nanoribbons. *ACS Nano* **4**, 1949–1954 (2010).

123. Georgakilas, V. *et al.* Multipurpose organically modified carbon nanotubes: From functionalization to nanotube composites. *J. Am. Chem. Soc.* **130**,

8733–8740 (2008).

124. Cioffi, C., Campidelli, S., Brunetti, F. G., Meneghetti, M. & Prato, M. Functionalisation of carbon nanohorns. *Chem. Commun.* 2129–2131 (2006). doi:10.1039/b601176d

125. Singh, R. *et al.* Tissue biodistribution and blood clearance rates of intravenously administered carbon nanotube radiotracers. *Proc. Natl. Acad. Sci. U. S. A.* **103**, 3357–3362 (2006).

126. Kostarelos, K. *et al.* Cellular uptake of functionalized carbon nanotubes is independent of functional group and cell type. *Nat. Nanotechnol.* **2**, 108–113 (2007).

127. Karousis, N., Tagmatarchis, N. & Tasis, D. Current progress on the chemical modification of carbon nanotubes. *Chem. Rev.* **110**, 5366–5397 (2010).

128. Tasis, D., Tagmatarchis, N., Bianco, A. & Prato, M. Chemistry of carbon nanotubes. *Chemical Reviews* **106**, 1105–1136 (2006).

129. Ballesio, A. *et al.* A novel hot embossing Graphene transfer process for flexible electronics. *Microelectron. Eng.* **209**, 16–19 (2019).

130. Parmeggiani, M. *et al.* A Novel Electrolyte Gated Graphene Field Effect Transistor on Cyclo Olefin Copolymer Foil. in *Proceedings of IEEE Sensors* **2018-October**, (Institute of Electrical and Electronics Engineers Inc., 2018).

131. Wang, Y. *et al.* The fabrication of Schottky photodiode by monolayer graphene direct-transfer-on-silicon. *J. Appl. Phys.* **128**, 014501 (2020).

132. Mazzaracchio, V. *et al.* Inside the different types of carbon black as nanomodifiers for screen-printed electrodes. *Electrochim. Acta* **317**, 673–683 (2019).

133. Wang, Y. ying *et al.* Raman Studies of Monolayer Graphene: The Substrate Effect. *J. Phys. Chem. C* **112**, 10637–10640 (2008).

134. Ferrari, A. C. Raman spectroscopy of graphene and graphite: Disorder, electron–phonon coupling, doping and nonadiabatic effects. *Solid State Commun.* **143**, 47–57 (2007).

135. Haddad, P.-A., Flandre, D. & Raskin, J.-P. A Quasi-Static Model of Silicon Substrate Effects in Graphene Field Effect Transistors. *IEEE Electron Device Lett.* **38**, 987–990 (2017).

136. Fisichella, G., Di Franco, S., Roccaforte, F., Ravesi, S. & Giannazzo, F. Microscopic mechanisms of graphene electrolytic delamination from metal substrates. *Appl. Phys. Lett.* **104**, 233105 (2014).

137. Lu, C.-C., Lin, Y.-C., Yeh, C.-H., Huang, J.-C. & Chiu, P.-W. High Mobility Flexible Graphene Field-Effect Transistors with Self-Healing Gate Dielectrics. *ACS Nano* **6**, 4469–4474 (2012).

138. Srinivasan, S. ELECTRODE/ELECTROLYTE INTERFACES: STRUCTURE AND KINETICS OF CHARGE TRANSFER. in *Fuel Cells* 27–92 (Springer US, 2006). doi:10.1007/0-387-35402-6_2

139. Meric, I. *et al.* Current saturation in zero-bandgap, top-gated graphene field-effect transistors. (2008). doi:10.1038/nnano.2008.268

140. Rocchitta, G. Buffers A guide for the preparation and use of buffers in biological systems.

141. Giacchetti, B. M. *et al.* CVD-grown graphene solution-gated field effect transistors for pH sensing. in *Materials Research Society Symposium Proceedings* **1283**, 34–39 (Cambridge University Press, 2011).

142. Liu, R. *et al.* Graphene plasmon enhanced photoluminescence in ZnO microwires. *Nanoscale* **5**, 5294–5298 (2013).

143. Ni, Z., Wang, Y., Yu, T. & Shen, Z. Raman spectroscopy and imaging of

graphene. *Nano Res.* **1**, 273–291 (2008).

144. Bie, Y. Q. *et al.* Site-specific transfer-printing of individual graphene microscale patterns to arbitrary surfaces. *Adv. Mater.* **23**, 3938–3943 (2011).
145. Cheung, S. K. & Cheung, N. W. Extraction of Schottky diode parameters from forward current-voltage characteristics. *Appl. Phys. Lett.* **49**, 85–87 (1986).
146. Dasaradha Rao, L., Shanthi Latha, K., Rajagopal Reddy, V. & Choi, C.-J. Effect of thermal annealing on the electrical and structural properties of Au/Y/p-type InP Schottky structure. *Vacuum* **119**, 276–283 (2015).
147. Li, X. *et al.* High Detectivity Graphene-Silicon Heterojunction Photodetector. *Small* **12**, 595–601 (2016).
148. Riazimehr, S. *et al.* Spectral sensitivity of a graphene/silicon pn-junction photodetector. in *EUROSOI-ULIS 2015 - 2015 Joint International EUROSOI Workshop and International Conference on Ultimate Integration on Silicon* 77–80 (Institute of Electrical and Electronics Engineers Inc., 2015). doi:10.1109/ULIS.2015.7063777
149. Xiang, D. *et al.* Surface Transfer Doping-Induced, High-Performance Graphene/Silicon Schottky Junction-Based, Self-Powered Photodetector. *Small* **11**, 4829–4836 (2015).
150. Yang, L., Yu, X., Xu, M., Chen, H. & Yang, D. Interface engineering for efficient and stable chemical-doping-free graphene-on-silicon solar cells by introducing a graphene oxide interlayer. *J. Mater. Chem. A* **2**, 16877–16883 (2014).
151. Feng, T. *et al.* Efficiency enhancement of graphene/silicon-pillar-array solar cells by HNO3 and PEDOT-PSS. *Nanoscale* **4**, 2130 (2012).
152. Miao, X. *et al.* High Efficiency Graphene Solar Cells by Chemical Doping. *Nano Lett.* **12**, 2745–2750 (2012).
153. An, X., Liu, F., Jung, Y. J. & Kar, S. Tunable graphene-silicon heterojunctions for ultrasensitive photodetection. *Nano Lett.* **13**, 909–916 (2013).
154. Aydin, H., Kalkan, S. B., Varlikli, C. & Celebi, C. P3HT-graphene bilayer electrode for Schottky junction photodetectors. *Nanotechnology* **29**, (2018).
155. Di Bartolomeo, A., Luongo, G., Iemmo, L., Urban, F. & Giubileo, F. Graphene-Silicon Schottky Diodes for Photodetection. *IEEE Trans. Nanotechnol.* **17**, 1133–1137 (2018).
156. OSA | High responsivity and bias-free graphene photodetector with nano-grating contact electrodes. Available at: https://www.osapublishing.org/abstract.cfm?uri=CLEO_QELS-2018-FTh4H.3. (Accessed: 3rd January 2021)
157. Liu, X. *et al.* Enhanced efficiency of graphene-silicon Schottky junction solar cells by doping with Au nanoparticles. *Appl. Phys. Lett.* **105**, 183901 (2014).
158. Shafique, S., Yang, S., Woldu, Y. T. & Wang, Y. Hierarchical synthesis of urchin-like V 2 O 5 hollow spheres and its photodetection properties. *Sensors Actuators, A Phys.* **288**, 107–116 (2019).
159. Shafique, S. *et al.* High-performance photodetector using urchin-like hollow spheres of vanadium pentoxide network device. *Sensors Actuators, A Phys.* **296**, 38–44 (2019).